Bathymetry from Space: White paper in support of a high-resolution, ocean altimeter mission

David T. Sandwell[1], Walter H. F. Smith[2], Sarah Gille[1], Steven Jayne[3], Khalid Soofi[4] and Bernard Coakley[5]

ABSTRACT

Perhaps the most important ocean science observation in the last two decades was provided by the Geosat radar altimeter during its 18-month geodetic mission (1985-86). The declassification of these data in July of 1995 set off a flurry of activity in basic research, industrial research/development, and public interest (Appendix A). While these data fill a huge gap in our understanding of the ocean basins, they also triggered a thirst for more. This paper reviews: i) the need for improved ocean bathymetry and gravity, ii) the fundamental physical limitations for recovering seafloor topography from measurements of ocean surface slope, and iii) the mission requirements to achieve significant improvements in accuracy and spatial resolution. While most areas of ocean science use bathymetric information, we focus on those applications where a new altimeter mission would provide the greatest benefit. These include:

- resolving the fine-scale (~15 km wavelength) tectonic structure of the deep ocean floor in areas that have not been surveyed by ships (e.g., abyssal hills, microplates, propagating rifts, seamounts, meteorite impacts, . . .);
- measuring the roughness spectra (15-100 km wavelength) of the seafloor on a global basis to better constrain models of tidal dissipation, vertical mixing, and mesoscale circulation of the oceans;
- and resolving the fine-scale (~15 km wavelength) gravity field of the continental margins for basic research and petroleum exploration.

Mission requirements for Bathymetry from Space are much less stringent and less costly than physical oceanography-type missions. Long-term sea-surface height accuracy is not needed; the fundamental measurement is the slope of the ocean surface to an accuracy of ~1 microradian. This can be achieved without application of the usual environmental corrections. The main requirements are improved altimeter range precision and dense coverage (< 7-km cross-track spacing) of the oceans for 6 years in order to reduce the noise from ocean waves, coastal tides, and mesoscale ocean variability. A low inclination orbit (50-65˚) is best for recovery of the low-latitude gravity field since the E-W slopes are poorly constrained by the Geosat and ERS altimeters. Existing and planned repeat-orbit altimeters will not achieve these objectives. Moreover, the satellite gravity missions, CHAMP, GRACE, and GOCE will recover sea surface slope at wavelengths greater than about 200 km but because of upward continuation, they cannot recover the shorter wavelengths. The primary science objective could be achieved with a relatively cheap mission. US petroleum exploration companies are keenly interested in these data, especially in coastal areas, and are willing to offer support for this mission.

[1]Scripps Institution of Oceanography, La Jolla, CA, 92093-0225; [2]Laboratory for Satellite Altimetry, NOAA, Silver Spring Maryland, 20910-3282; [3]CIRES and Dept. of Physics, Univ. of Colorado, Boulder, CO 80309-0216; [4]Conoco Inc., 600 North Dairy Ashford, Houston, TX, 77252-2197; Dept. of Geology, Tulane Univ., New Orleanes, LA 70118.

1. INTRODUCTION

A detailed knowledge of the topography of the Earth is fundamental to the understanding of most Earth processes. On the land, weather and climate are controlled by topography on scales ranging from large continental landmasses to small mountain valleys. Since the land is shaped by tectonics, erosion, and sedimentation, detailed topography is essential for any geological investigation. In the oceans, detailed bathymetry is also essential for understanding physical oceanography, biology, and marine geology. Currents and tides are steered by the overall shapes of the ocean basins as well as by the smaller sharp ocean ridges and seamounts. Recent publications suggest that the interaction of tides and currents with the rugged seafloor mix the ocean to provide a global overturning. Sea life is abundant where rapid changes in ocean depth deflect nutrient-rich water toward the surface. Because erosion and sedimentation rates are low in the deep oceans, detailed bathymetry also reveals the mantle convection patterns, the plate boundaries, the cooling/subsidence of the oceanic lithosphere, the oceanic plateaus, and the distribution of volcanoes.

Topographic mapping with orbiting laser and radar altimeters has been the focus of current exploration of Venus, the Moon, and Mars and is providing very high resolution topographic maps of the Earth's land areas. However, since one cannot directly map the topography of the ocean basins from space, most seafloor mapping is a tedious process that has been carried out over a 40-year period by research vessels equipped with single or multibeam echo sounders (Figure 1.1).

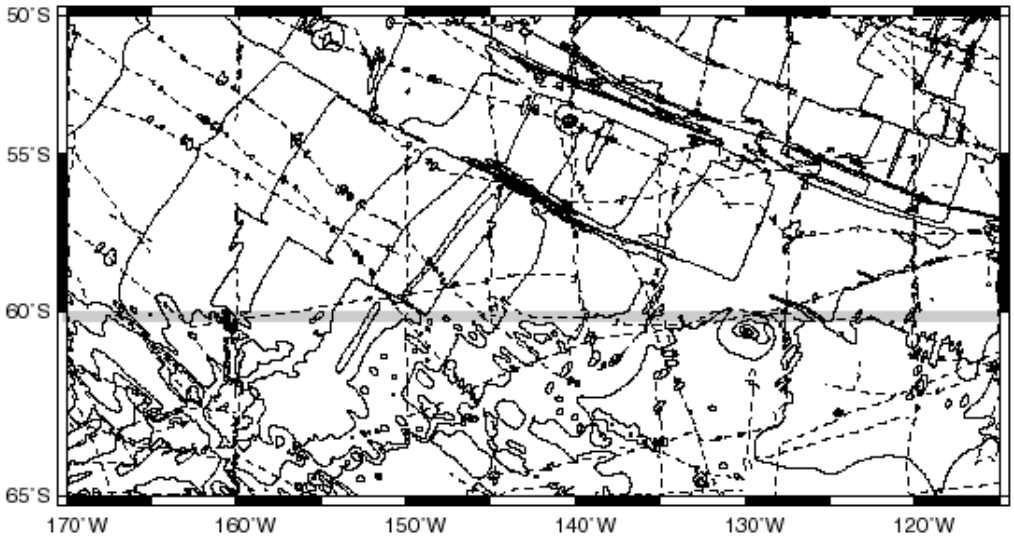

Figure 1.1 A hand-drawn contour map (500 m contour interval) of a portion of the South Pacific Ocean along the Pacific-Antarctic Rise from the GEBCO Digital Atlas [*Jones et al.,* 1997]. Note that depth contours show "zigzags" even in the absence of supporting trackline control (dashed lines), apparently to portray offsets in depth implied at inferred fracture zones. A substantial increase in the roughness of the seafloor south of the 60°S parallel is also apparent; many more seamounts are drawn, including many for which no supporting data are in evidence. This artificial change in roughness at 60°S occurs because one individual contoured the northern section while a second individual contoured the southern section.

Problems with Topographic Maps of the Ocean Floor

Current maps of the seafloor based on shipboard soundings suffer from three problems: irregular data distribution, poor quality of unique soundings in remote areas, and archaic methods of map production. The global distribution of available data is irregular, with many gaps between surveys; these are often as large as 10^5 km^2, or roughly the size of the State of Oklahoma in the United States. In addition, the resolution and accuracy of the data are variable [*Smith*, 1993]. Most of the data in remote ocean basins were collected during an era of curiosity-driven exploration (1950 – 67), depths were measured by single-beam analog echosounders, and satellite navigation was unavailable. Recent surveys using advanced technology (i.e., GPS navigation and multi-beam acoustic swath mapping systems) are funded through a peer-review system emphasizing hypothesis testing; the result is that ships tend to re-visit a limited number of localities. Thus the majority of the data in the remote ocean basins are old and of poor quality. These remarks apply to data that are publicly available; additional data exist that are proprietarily held for commercial or political reasons, or are classified as secret for military purposes. The largest such data set, the Ocean Survey Program of the U.S. Navy, covers primarily the northern oceans [*Medea*, 1995].

In addition to the irregular distribution and quality of the existing soundings, the data compilation methods are heterogeneous and can contain significant biases (Figure 1). Synthesis of depth soundings into representations of topography has traditionally been done by bathymetrists who draw contour maps by hand to portray inferred sea floor morphology [*Canadian Hydrographic Service*, 1981]. While the maps have been of enormous value in portraying the general outline of features and stimulating research, they have also compounded the heterogeneity in the data by adding the idiosyncrasies of each bathymetrist's interpretation to the already difficult problem of the data quality and distribution of shipboard bathymetry.

Contour maps such as these have been digitized and then gridded to produce digital elevation models (DEMs) of the sea floor; the most widely used product began in the U.S. Navy as "SYNBAPS" (Synthetic Bathymetric Profiling System [*Van Wyckhouse*, 1973]) and then "DBDB-5" (Digital Bathymetric Data Base on a 5 arc-minute grid) and was eventually distributed as "ETOPO5" (Earth Topography at 5 arc-minutes) [*National Geophysical Data Center*, 1988]. These products, like all DEMs made from digitized contours, suffer statistical biases and other artifacts that are inevitable consequences of the contour interpolation process. The most common problem, called "terracing", is that depth values equal to contour levels occur much more frequently than any other values; *Smith* [1993] has shown that this error leads to a bias in geophysical parameters estimated from ETOPO5 data.

In summary, the distribution of bathymetric data is uneven and leaves gaps of many hundreds of km; it is biased toward the northern oceans; the bias is even more pronounced in the accurately navigated and digitized data; global syntheses are a "patchwork quilt" of idiosyncratic human interpretations; and additional artifacts and statistical problems are present in global bathymetry in the form of DEMs. This state of things will continue into the foreseeable future, because the cost of doing a globally uniform survey exceeds the political will to do so. It has been estimated that the 125--200 ship-years of survey time needed to map the deep oceans at 100 m resolution would cost a few billion US$, and mapping the shallow seas would take much more time and funding [*M. Carron, U.S. Naval Oceanographic Office, pers. commun.* 2001].

While shipboard surveys are the only means for high-resolution (200 m wavelength) seafloor mapping, moderate resolution (15-25 km wavelength) can be achieved using satellite radar altimetry at a

fraction of the cost. Radar altimeters aboard the ERS-1 and Geosat spacecraft have surveyed the marine gravity field over nearly all of the world's oceans to a high accuracy and moderate spatial resolution. These data have been combined and processed to form a global marine geoid and gravity grid [*Cazenave et al.*, 1996; *Sandwell and Smith*, 1997; *Tapley and Kim*, 2001]. (Appendix B briefly describes the theory for calculating the gravity anomaly from the gradient of the ocean surface.) In the wavelength band 10 to 160 km, variations in gravity anomaly are highly correlated with seafloor topography and thus, in principle, can be used to recover topography (Appendix C). There are ongoing efforts to combine ship and satellite data to form a uniform-resolution grid of seafloor topography [Figures 1.2 and 1.3] [*Baudry and Calmant*, 1991; *Jung and Vogt*, 1992; *Calmant*, 1994; *Smith and Sandwell*, 1994; *Sichoix and Bonneville*, 1996; *Ramillien and Cazenave*, 1997; *Smith and Sandwell*, 1997]. The sparse ship soundings constrain the long wavelength (> 160 km) variations in seafloor depth and are also used to calibrate the local variations in topography to gravity ratio associated with varying tectonics and sedimentation. Current satellite-derived gravity anomaly provides much of the information on the intermediate wavelength (24-160 km) topographic variations. The main limitation is the noise in the gravity anomaly measurements (i.e., sea surface slope) since this becomes amplified during the downward continuation process. The bathymetric models can only be improved through more accurate and dense measurements of the ocean surface slope or complete multibeam echo sounding of the seafloor (Appendix C.).

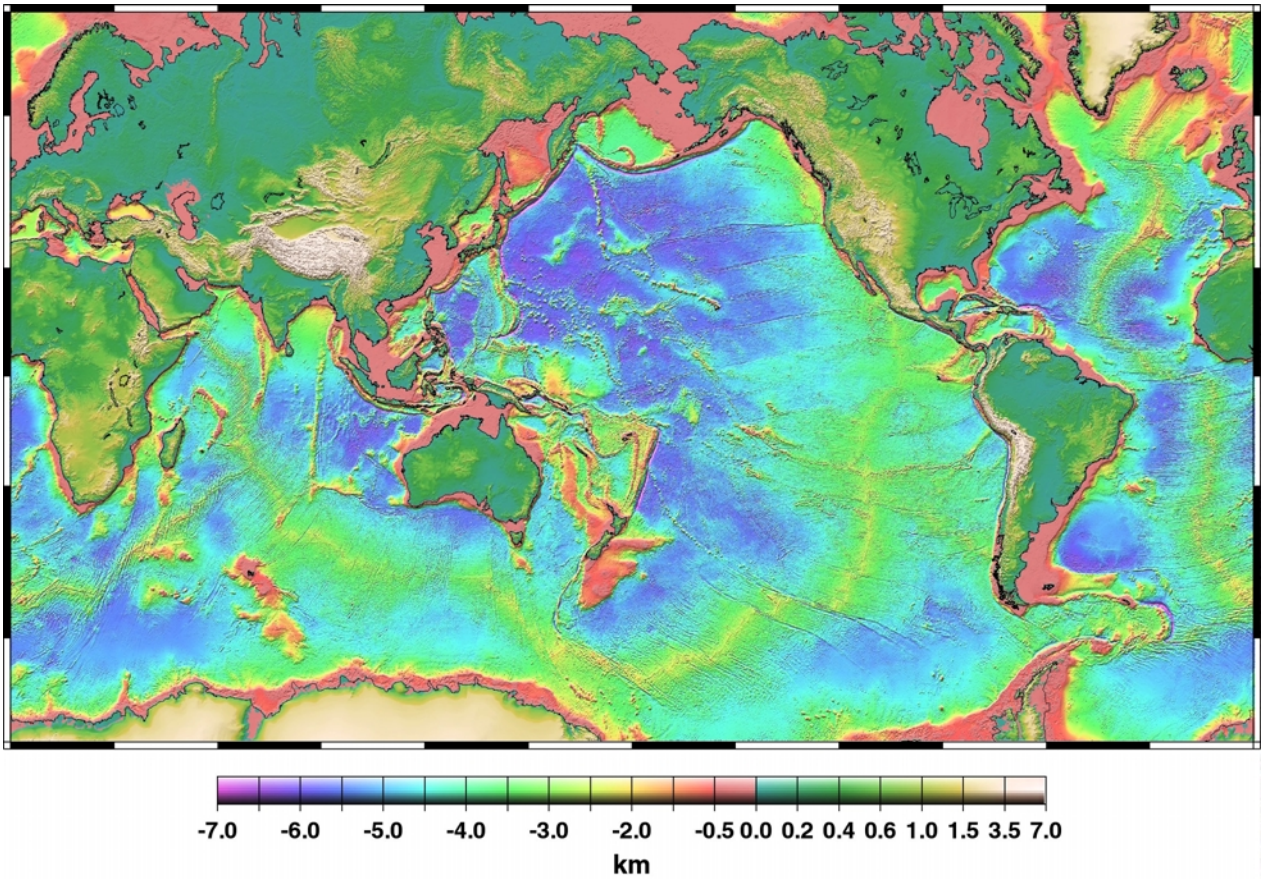

Figure. 1.2 Global map of predicted seafloor depth [*Smith and Sandwell*, 1997] and elevation from GTOPO-30.

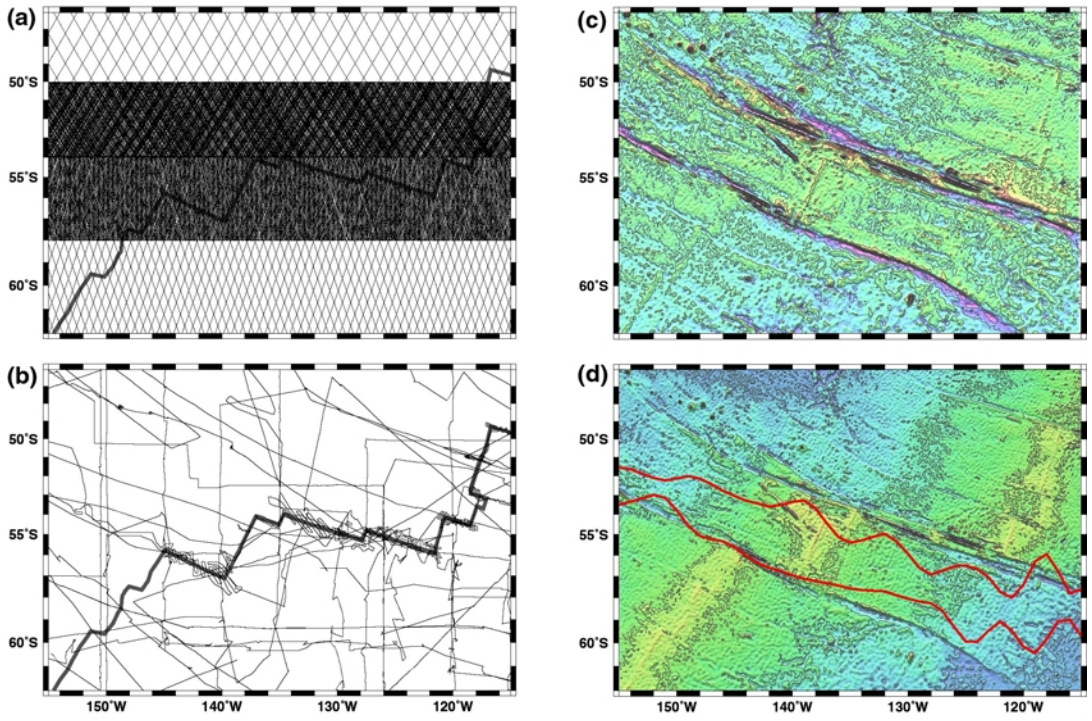

Figure 1.3 (a) Tracks of stacked Geosat/ERM (17-day repeat cycle), Geosat/GM, ERS-1 Geodetic Phase (168-day repeat cycle) and stacked ERS-1 (35-day repeat). (b) Ship tracks in area of the Eltanin and Udintsev transform faults. Track density is sparse except along the Pacific-Antarctic plate boundary. (c) Gravity anomaly (mGal) derived from all 4 altimeter data sets. (d) Bathymetry (m) estimated from ship soundings and gravity inversion. Red curves mark the sub-Antarctic and polar fronts of the Antarctic Circumpolar Current [*Gille*, 1994]. The Sub-Antarctic Front (SAF-red) passes directly over a NW-trending Hollister ridge which has a minimum ocean depth of 135 m [*Geli et al*., 1997]. The Polar Front (PF) is centered on the 6000m deep valley of the Udintsev transform fault.

This paper provides the scientific rationale (Section 2) for proposing a new satellite altimeter mission. While bathymetric information is used for a wide variety of ocean research, we focus on those applications where a new altimeter mission would provide the greatest benefit. These include resolving the fine-scale (~15 km wavelength) tectonic structure of the deep ocean floor (e.g., abyssal hills, microplates, propagating rifts, seamounts, meteorite impacts, . . .); measuring the roughness spectra (15-100 km wavelength) of the seafloor on a global basis to better constrain models of tidal dissipation, vertical mixing, and mesoscale circulation of the oceans; and resolving the fine-scale (~15 km wavelength) gravity field of the continental margins for basic research and petroleum exploration. Section 3 reviews the limitations of past, current, and planned altimeter missions to confirm that a new mission is needed to achieve the science objectives. The current average resolution of the ocean surface slope and topography is about 24 km which insufficient to resolve even the largest components of the ubiquitous fabric of the ocean floor (abyssal hills). A significant portion of the abyssal hill spectrum occurs in the 15 to 24 km wavelength band that we hope to resolve with a new system. Section 4 outlines a doable altimeter mission that would achieve many of the science objectives at a low cost compared with previous radar altimeter missions. The 15 km resolution objective can be achieved by

improving the accuracy of the global ocean surface slope measurement by a factor of 4. A factor of 2 can be achieved with a new altimeter design and another factor of 2 can be achieved with a 6-year long mission. Four appendices provide backup information related to technical details. Since the objectives of this mission are considerably different from typical repeat-pass oceanographic altimeter missions, it is important to demonstrate that features such as a dual-frequency altimeter would not increase the precision of the basic slope measurement and are thus an unnecessary component of a new mission.

Table 1. Applications of High Spatial Resolution Satellite Altimetry

Topography Applications:

- fiber optic cable route planning (http://oe.saic.com)
- tsunami models (Yeh, 1998)
- hydrodynamic tide models, tidal friction, and stirring of the oceans [Jayne & St. Laurent, 2001]
- improvement of coastal tide models [*Shum et al.,* 1997; 2000]
- ocean circulation models [Smith et al., 2000; R. Tokmakian, pers. commun.]
- understanding seafloor spreading ridges [*Small,* 1998]
- identification of linear volcanic chains [*Wessel and Lyons,* 1997]
- education and outreach (i.e. geography of the ocean basins)
- law of the sea [Monahan et al., 1999]

Gravity Applications:

- inertial guidance of ships, submarines, aircraft, and missiles
- planning shipboard surveys
- mapping seafloor spreading ridges and microplates (http://ridge.oce.orst.edu)
- establishing the structure of continental margins (http://www.ldeo.columbia.edu/margins/Home.html)
- petroleum exploration (Section 2.4)
- plate tectonics [*Cazenave and Royer,* 2001]
- strength of the lithosphere [*Cazenave and Royer*, 2001]
- search for meteorite impacts on the ocean floor [*Dressler and Sharpton,* 1999]

2. SCIENTIFIC RATIONALE FOR A BATHYMETRIC ALTIMETER MISSION

While these satellite-derived maps of marine gravity anomaly and seafloor topography have sufficient accuracy and resolution for certain applications (Table 1), there are several important science questions that can only be addressed with better accuracy and resolution. Here we focus on three science issues but note that seafloor topography is fundamental to all aspects of ocean science.

What is the fine-scale tectonic structure of the deep ocean?

How does seafloor depth and seafloor roughness affect ocean circulation and deep ocean mixing?

What is the sedimentary and crustal structure of the continental margins?

2.1 *Cause and characterization of seafloor roughness*

Satellite altimetry has revealed the large-scale manifestations of plate tectonics such as seafloor spreading ridges, transform faults, fracture zones, and linear volcanic chains (Figure 1.2) [*Haxby et al.*, 1983; ; *Gahagan et al.*, 1988] and ridges [*Smith and Sandwell*, 1994], allowing refinement of the history of plate tectonic motions [e.g., *Shaw and Cande*, 1990; *Mayes et al.*, 1990; *Müller and Smith*, 1993]. While altimetry has furnished a spectacular confirmation of the plate tectonic theory, the dense altimeter data available since 1995 have also shown that there are many complex details of plate tectonics that are poorly understood. Here we focus on those processes that produce smaller scale sea floor topography and structure in the oceanic crust.

Until dense altimeter data over ridges became available, many seafloor spreading studies were focused on the East Pacific Rise and the Mid-Atlantic Ridge and the differences in their bathymetric morphology: the EPR has an axial summit and relatively smooth flanks, while the MAR has a deep median valley and rougher flanks [*Menard*, 1958; *Heezen et al.*, 1959; *Menard*, 1964]. The lengths of axis segments and their offsets at transform faults also differ from one ridge to the other [*Abbott*, 1986]. The differences are manifest in gravity anomalies as well [*Menard*, 1967; *Cochran*, 1979; *Macdonald et al.*, 1986] and thus show up in satellite altimeter data [*Small & Sandwell*, 1989; 1994]. Figure 2.1 (left) shows topography and gravity profiles across these two ridges. The EPR has a smooth gravity profile with a positive anomaly over the axis of 10 or more mGal, while the MAR has a rougher gravity profile with a negative anomaly over the axis exceeding 30 mGal in magnitude.

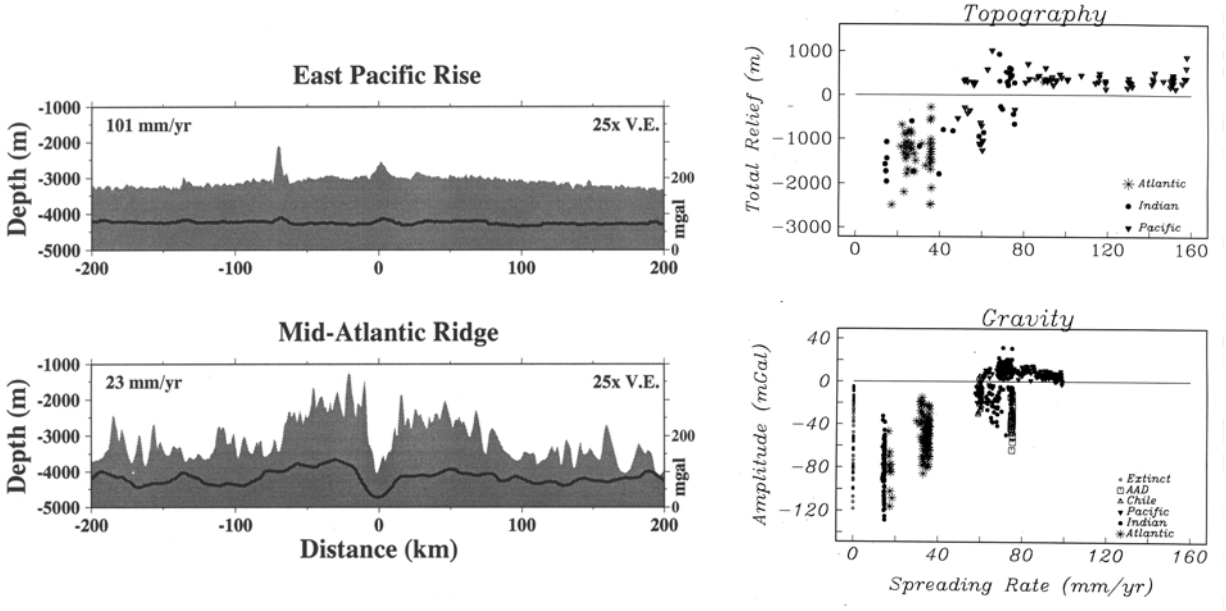

Figure 2.1 Typical ridge axis relief and gravity amplitude versus spreading rate [*Small*, 1994].

Plate tectonics explains that the MAR spreading rate is relatively slow (23 mm/yr. full-rate) while the EPR spreading rate is relatively fast (101 mm/yr. full-rate), and so a number of models have been proposed to explain the contrasting characters in terms of spreading-rate-dependent material strength and the transience or permanence of a magma supply [*Sleep,* 1969; *Tapponier & Francheteau,* 1978*; Phipps Morgan et al.,* 1987]. Analysis of repeat-track Geosat profiles over ridges revealed an abrupt transition in ridge-axis gravity with spreading rate which occurs at a full-rate of about 80 mm/yr [*Small and Sandwell,* 1989; 1992]. These observations prompted the development of models for an abrupt transition in axial morphology [*Chen & Morgan,* 1990a, 1990b; *Phipps Morgan & Chen,* 1992, 1993]. Studies of shipboard bathymetric profiles [*Malinverno,* 1991; *Small,* 1998] were limited by the limited geographical distribution and heterogeneity in these data, and altimeter data provided a more uniform and systematic view (Figure 2.1).

The gravity roughness results were extended beyond the ridge axes to the entire ocean basins [*Smith,* 1998] by accounting for the variation in anomaly amplitude with depth to the sea floor (Appendix C). This accounting requires "downward continuation", which is unstable in the presence of noise in the data (Figure C4 of Appendix C). The global gravity roughness is combined with the seafloor age [*Müller et al.,* 1997] to produce roughness versus spreading rate (Figure 2.2). Since this figure, obtained from data throughout the ocean basins, shows the same pattern as one finds over ridge axes, *Smith* [1998] concluded that the seafloor spreading process is responsible for the short-wavelength roughness of the seafloor everywhere, not just on ridge axes.

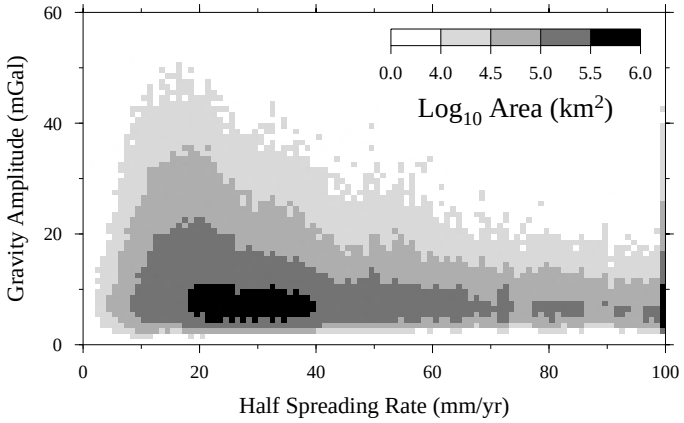

Figure 2.2 Histogram of global sea floor area in bins of 1 mm/year half-spreading rate and 1 mGal gravity roughness amplitude. The largest amplitudes are found at half-rate less than 20 mm/yr. and large amplitudes are uncommon at half-rates greater than 50 mm/yr. Amplitudes less than 3 mGal rarely occur, reflecting the noise level in the altimeter data.

As dense altimeter data became globally available they revealed details in the seafloor spreading process, including propagating rifts [*Phipps Morgan & Sandwell,* 1994], non-transform ridge offsets [*Lonsdale,* 1994], ridge-hotspot interactions [*Small,* 1995], disorganized back-arc spreading [*Livermore*

et al., 1994], small (20 km) ridge jumps [*Marks & Stock*, 1995], and small scale (circa 25 km) spreading-rate-dependent tectonic fabric [*Small & Sandwell,* 1994; *Marks & Stock,* 1994; *Phipps Morgan & Parmentier*, 1995; *Sahabi et al.,* 1996]. *Phipps Morgan & Parmentier* [1995] interpret a new fabric they call "crenulated seafloor" as evidence for stationary and/or migratory localized centers of upwelling magma beneath ridges. Many of these kinds of features are symmetric across ridge flanks, and many can be seen in Figure 2.3.

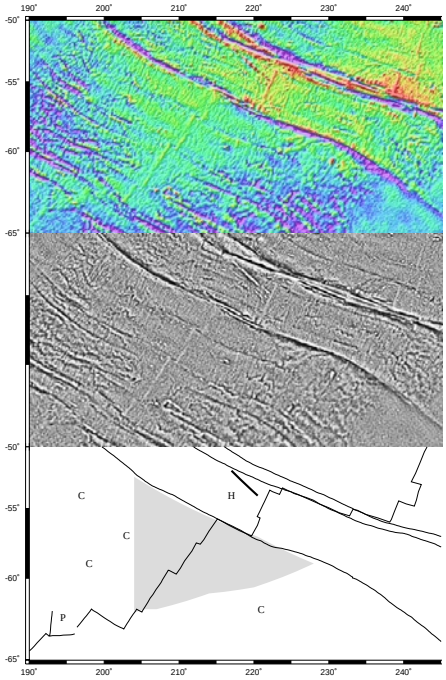

Figure 2.3 Three maps of an area on the Pacific-Antarctic Ridge (upper right to lower left in each panel). Top: gravity anomalies from satellite altimetry. Middle: satellite altimeter data processed to enhance tectonic fabric. Bottom: key to features. P = small propagating rift trace. H = Hollister ridge, a seismically and volcanically active but previously unmapped feature [*Geli et al.,* 1997]. C = areas with chaotically wandering structures. Inside the gray zone, ridge axis offsets are few and fabric is smooth, although perhaps regularly crenulated, with few fracture zones or other fossil traces of axial disturbances; this is the morphology typical of fast spreading ridges such as the East Pacific Rise. Outside the gray zone, the fabric is the opposite and is that typical of slow spreading ridges such as the Mid-Atlantic Ridge. The wedge shape of the gray zone shows that the transition from one style to the other has propagated southwesterly along the ridge.

Seafloor structure at quite small spatial scales (0.2-10 km wavelength) has also been imaged in acoustic swath bathymetry but only in a few small patches. *Goff & Jordan* [1988] found that the very small scale seafloor topography is self-affine, and can be characterized statistically in terms of a simple model in which the power spectrum of the topography has three characteristic parameters: an amplitude of the total root-mean-square roughness, the slope in the roll-off in the short wavelength part of the spectrum and the corner wavenumber. To assess the capabilities of current and future bathymetric prediction from a new satellite altimeter mission, we have assembled three 200 km by 200 km areas where multibeam bathymetry data are available. The current and future capabilities will be discussed in Section 3 below. Here we illustrate the major differences in seafloor characteristics in these areas

(Figure 2.4). The Mid-Atlantic Ridge (MAR) is characterized by an axial valley with relatively rugged surrounding seafloor abyssal hills (493 m rms). The hills are very anisotropic with the long-axis perpendicular to the seafloor spreading direction and visually have a characteristic wavelength of about 10 km. The Pacific Rise (EPR) has similar but lower amplitude abyssal hill; the total roughness is only 209 m reflecting its higher spreading rate. The Gulf of Mexico has quite different seafloor morphology with a more isotropic pattern which formed in response to buoyancy instabilities of salt domes. Spectra for the MAR and EPR are provided in Figure 2.5b. The amplitudes of the spectra are different but their corner frequency and roll-off slope are similar. Other areas such as the Southwest Indian Ridge studied by *Goff and Jordan* [1988] has more total power (845 m) and a somewhat longer corner wavenumber of about 50 km. *Smith* [1998] found that amplitudes and wavelengths of abyssal hills along the MAR are just large enough to be barely resolved in existing altimeter data over water as deep as 4 km.

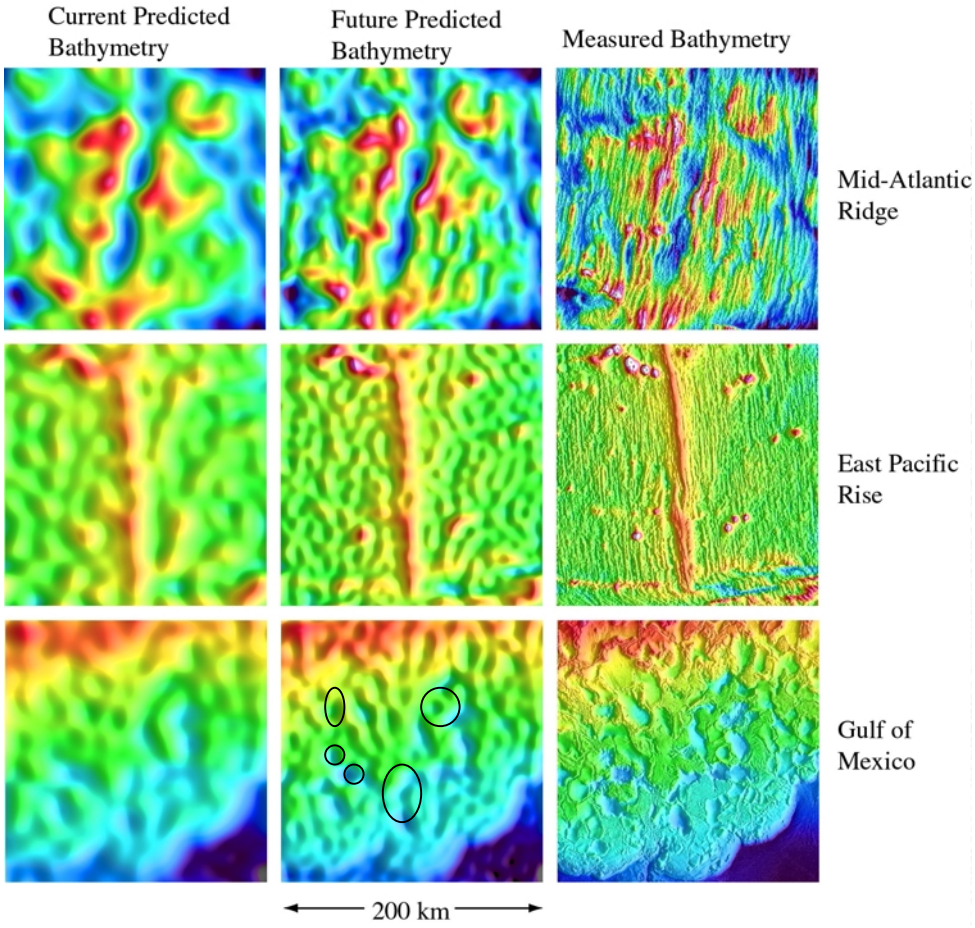

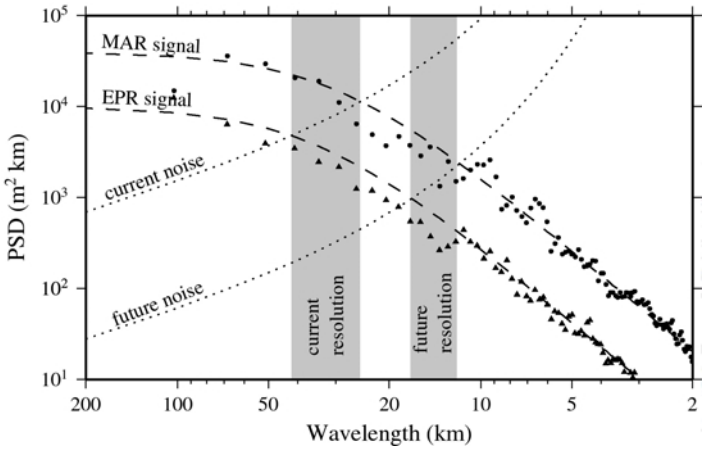

Figure 2.4 (upper) Measured bathymetry (right column) and predicted bathymetry (left and center columns) for representative areas on the Mid-Atlantic Ridge, the East Pacific Rise, and the Gulf of Mexico. The Mid-Atlantic Ridge and East Pacific Rise show the characteristic abyssal-hill signature of slow and fast spreading ridges, respectively. The current prediction assumes a 5 mGal noise level reflecting the current accuracy of the altimeter-derived gravity. This must be low-pass filtered at a wavelength of 24 km to avoid the amplification of the noise by downward continuation. The future predicted bathymetry assumes a 1 mGal noise level and uses a 15 km wavelength low-pass filter. While the current prediced bathymetry in the Gulf of Mexico is unable to resolved the salt-related mini-basins (outlined), the future predicted bathymetry reveals some of the more important structures; a global data set would be beneficial in frontier reconnaissance studies (see Section 2.4)

(lower) East-west spectra of the Mid-Atlantic Ridge and the East Pacific rise area bathymetry. For both areas, the corner wavenumber and roll-off exponent are 20 km and –2.8, respectively. The total power is 493 m for the MAR and 209 m for the EPR. The noise spectra (dotted curves) for current and future bathymetric prediction is discussed in the following section. A signal to noise ratio of 1 reflects the resolution limits of current and future bathymetric prediction. The current resolution for rough and smooth seafloor is 25 km and 45 km , respectively. Assuming a factor of 5 noise reduction in a future mission, the resolution improves to 12 and 17 km, respectively. Note this improvement brackets the corner wavenumber of 20 km.

2.2 *Tidal dissipation and deep ocean mixing*

Tides are the major process responsible for mixing the deep ocean. Astronomical calculations suggest that tidal mixing should dissipate 3.7 terawatts (TW) of energy throughout the global ocean. *Munk and Wunsch* [1998] estimated that about 1.9 TW of this tidal energy are required to maintain the observed deep ocean stratification. While tidal processes are known to be important in coastal regions and marginal seas [*Shum et al.,* 1997; 2001], tidal dissipation due to shallow ocean boundary layer effects does not account for all tidal dissipation. *Egbert and Ray* [2000] estimated that 25% to 30% of total tidal dissipation takes place in the open ocean, and is generally associated with ridges and other rough topography.

Recent observational efforts have attempted to measure the effect of open ocean tidal dissipation and its corresponding impact on vertical diffusivities in the ocean. In microstructure measurements in the Brazil Basin (Figure 2.5), *Polzin et al.* [1997] found elevated levels of vertical diffusivity over rough bathymetry. Diffusivity levels appear to be modulated by the fortnightly and monthly tidal cycle [*Ledwell et al.,* 2000]. These results are consistent with the idea that tidal motions over rough

bathymetry generate vertically propagating internal waves that dissipate tidal energy and vertically mix the ocean.

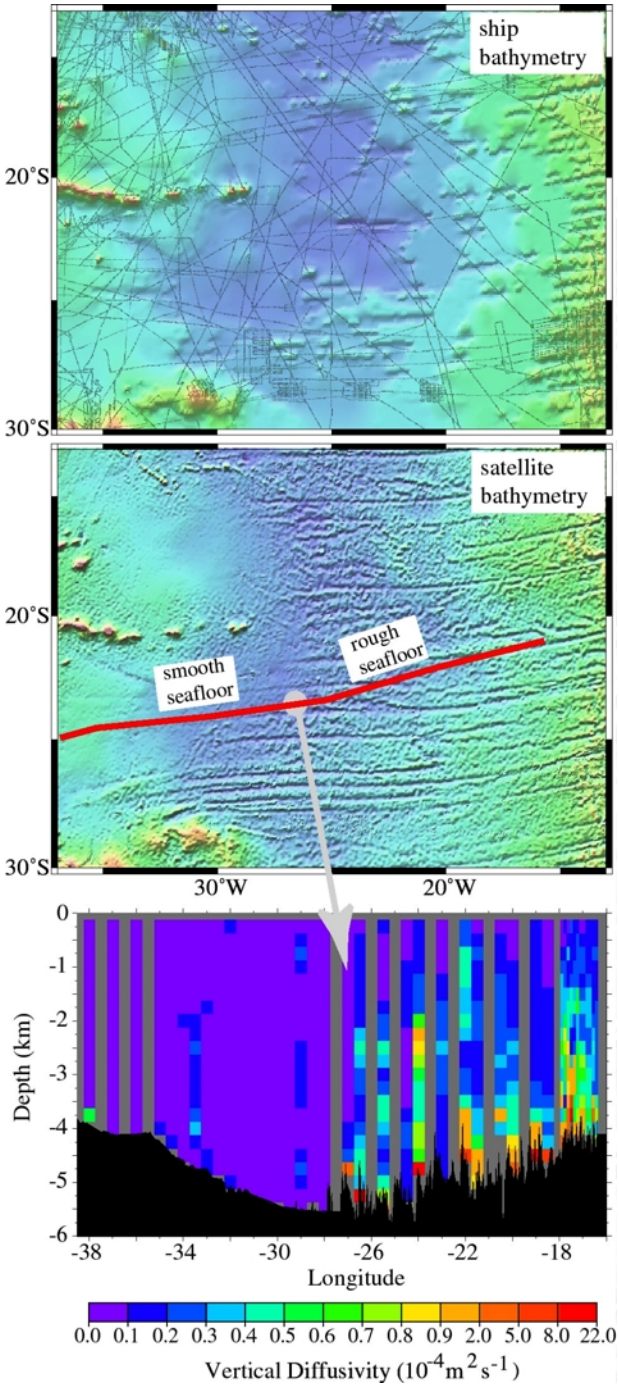

Figure 2.5 (upper) Bathymetry of Brazil Basin, South Atlantic derived from ship soundings lacks the resolution needed to distinguish between rough and smooth seafloor. (center) Bathymetry derived from satellite altimetry and ship soundings resolves the rough seafloor associated with fracture zones but not abyssal hills. (lower) Vertical diffusivity represents vertical mixing of stratified seawater. Mixing rates are an order of magnitude greater over rough topography (abyssal hills and fracture zones) than they are over smooth topography. Enhanced mixing over rough topography extends from depths of about 1500 m to the bottom of the ocean (> 4000 m). Mixing effects the vertical stratification which in turn influences deep currents and their horizontal and vertical stability to perturbations (after *Polzin et al.* [1997]).

To test the impact of bathymetric roughness on tides, *Jayne and St. Laurent* [2001] implemented a roughness dependent internal-wave drag term in a barotropic tide model. Figure 2.7 compares tidal dissipation in two versions of the model. Panel (a) has only standard bottom drag; panel (b) includes internal-wave drag using roughness calculated from *Smith and Sandwell* [1997] bathymetry (Figure 2.8); and panel (c) shows the differences between the two. The inclusion of internal-wave drag results in substantially more dissipation, particularly in the middle of ocean basins. Jayne and St. Laurent found that the rms difference between observed and modeled tides was 40% smaller when they included a roughness dependent dissipation term. In addition, in agreement with *Egbert and Ray's* [2000] observations, deep-ocean tidal dissipation due to the roughness term was about 30% of total dissipation.

In this model, viscous drag in the deep ocean is primarily due to generation (and subsequent dissipation breaking) of internal waves with the following parameterization $(1/2)\kappa h^2 N\mathbf{u}$ where $\mathbf{u}$ is the fluid velocity vector, N is the buoyancy frequency [*Levitus et al.*, 1994], h is the seafloor roughness, and κ is 2π/wavelength of the topography. Using the bathymetric roughness derived from predicted bathymetry (Figure 2.8), *Jayne and St Laurent* [2001] find that internal waves are primarily excited by topography at wavelengths of 10 km. However, it should be noted that the roughness variations from the predicted bathymetry are underestimated by perhaps a factor of 2 because the resolution is limited to about 24 km wavelength and the noise in the gravity field propagates into bathymetric noise. The drag contribution depends on the product of the roughness squared and the wavenumber so increasing the roughness will reduce the excitation wavenumber (i.e., increase the wavelength). A more complete description of this process will require bathymetric roughness spectra over wavelengths of 10 to 30 km [Steven Jayne, personal communication, 2001]; note this corresponds to the ubiquitous abyssal hill topography described above. These are also the wavelengths that are not currently resolved in the predicted bathymetry (Figure 1.2). While these models are still under development and there is some debate about the physics of the internal-wave generation process, numerical simulations are hampered by the lack of high-resolution seafloor bathymetry.

The role of topography in tidal mixing and internal wave generation remains an active area of research in physical oceanography. Underway now is the Hawaii Ocean Mixing Experiment (HOME) [http://chowder.ucsd.edu/home/home.html], a large field program with two dozen investigators. HOME specifically focuses on observing and modeling mixing along the Hawaiian Ridge. HOME is directed towards understanding specific processes, including the impact on tidal conversion of critical bottom slopes over length scales of 1 km or less [*R. Pinkel, personal communication*]. Although such length scales are beyond the reach of altimetry, the lessons learned in HOME appear likely to translate into ways to characterize ocean mixing on the basis of larger scale bathymetry.

A new higher-resolution altimetric bathymetry (10-30 km wavelength) would offer the potential to better refine ocean mixing estimates, extending the results from the Brazil Basin, HOME and other field programs to give them global applicability and making the existing global roughness estimates more reliable. Of particular interest is the western Equatorial Pacific, near the Solomon Islands, a region that is not well mapped but where seamounts and ridges associated with the island chains may substantially influence mixing processes.

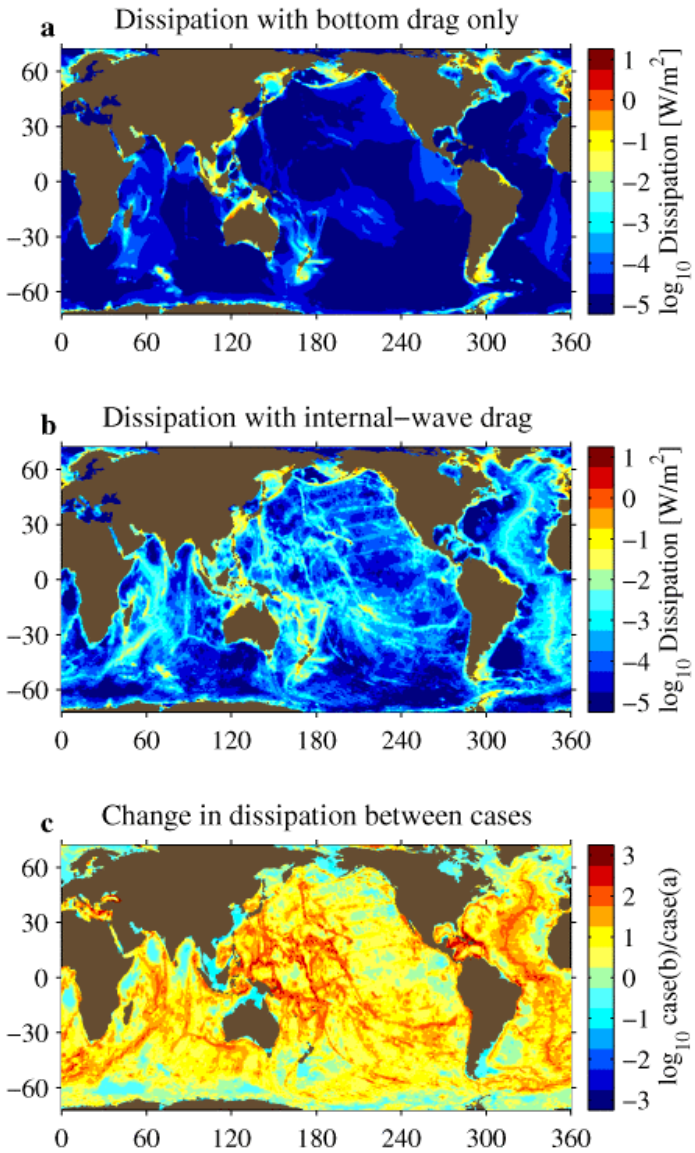

Figure 2.7 Tidal dissipation due to bottom drag alone, (a), is insufficient to explain total observed dissipation. Including additional dissipation scaled to bottom roughness to simulate internal mixing, (b), changes the model (c) and brings it more in line with observed data. After *Jayne & St. Laurent* [2001].

2.3 *Ocean circulation and mesoscale eddie*s

Ocean circulation is influenced by seafloor topography in a variety of ways, particularly at high latitudes, where stratification is low. Bathymetry can steer the path of currents, determine where upwelling occurs (and supply iron-rich sediment to upwelled water allowing phytoplankton to bloom at the ocean surface), generate topographic lee waves downstream of topography, and dissipate eddy kinetic energy.

Theoretical constraints on vorticity suggest that large-scale barotropic flows in the ocean should be directed along lines of constant *f/H*, where *f* is the Coriolis parameter and *H* is the ocean depth. At high-latitudes where changes in *f* are small, barotropic oceanic flows should nearly follow bathymetric contours. Although real flows include baroclinic components and are expected to deviate from *f/H* lines,

bathymetry is nonetheless a good predictor for large-scale circulation patterns. *LaCasce* [2000] showed that in both the Atlantic and Pacific Oceans, floats were more likely to travel along *f/H* contours than across them. *Holloway* [1992] has even suggested that topography should be used as an a priori guess to determine large-scale dissipation in ocean circulation models.

Specific current flow patterns are clearly determined by bathymetry. For example, the path of the wind-driven Antarctic Circumpolar Current (ACC) has long been known to be steered by deep seafloor topography [e.g., *Gordon and Baker,* 1986] (Figure 1.3). Altimetric investigations suggest that the jets that comprise the ACC are tightly steered around bathymetric obstructions in the Southern Ocean. Figure 2.8 shows that the paths of the Subantarctic Front and Polar Front (as estimated from altimetry) pass through the Eltanin and Udintsev Fracture Zones, respectively, in the Pacific-Antarctic Ridge [*Gille,* 1994]. Similar effects occur downstream of Drake Passage and south of New Zealand, where the ACC is steered through troughs between a series of islands. Detailed study of the role that bathymetry plays in controlling ocean circulation has been limited by the lack of accurate bathymetry, particularly in the Southern Ocean where areas as large as $2x10^5$ km^2 are unsurveyed [*Sandwell and Smith,* 2001] and where current altimetric bathymetry cannot resolve all of the details of the bathymetry.

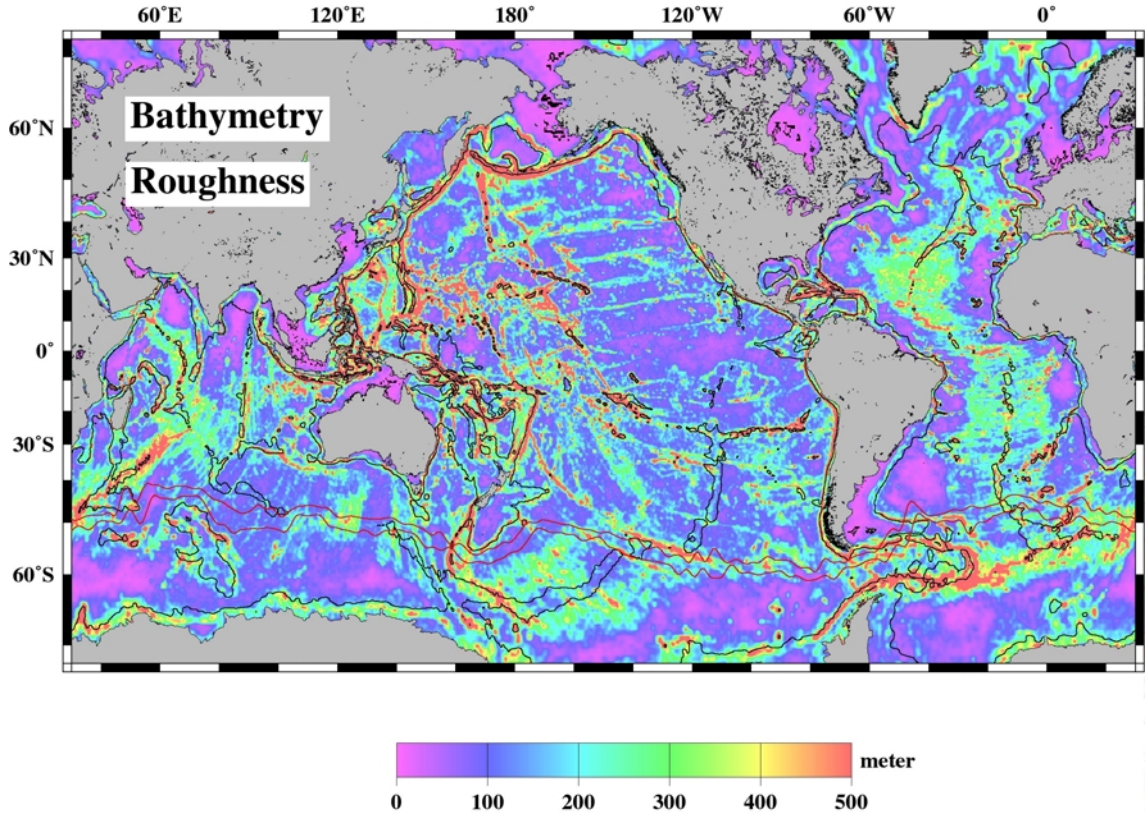

Figure 2.8 Seafloor roughness from altimeter-derived, high-pass filtered topography (24-160 km wavelength). Because of noise in the gravity field, the smaller-scale seafloor roughness associated with abyssal hills is not captured in this estimate. Analysis of high-resolution bathymetry suggests that the ratio of rough-to-smooth seafloor is at least two times greater than shown in this figure.

Ridges can generate topographic lee waves [e.g. *McCartney*, 1976]. Altimeter observations have consistently shown elevated levels of eddy kinetic energy downstream of ridges and seamounts, in the Gulf Stream [*Kelly*, 1991] and particularly in the ACC [*Sandwell and Zhang*, 1989, *Chelton et al.*, 1990; *Morrow et al.*, 1992; *Gille and Kelly*, 1996]. In an analysis based on sea surface height variability estimates from altimeter data, *Stammer* [1998] found evidence for high meridional eddy heat fluxes in locations of high eddy kinetic energy, suggesting that high variability regions associated with topography are potentially important in the global heat budget.

Topography also plays a role in vertical motions in the ocean. Horizontal flow that encounters topography can be deflected vertically rather than around topography. At George's Bank, tidal forcing over topography upwells water to the surface. In the equatorial Pacific, topography plays a slightly different role: upwelling is driven by a wind divergence at the equator rather than topography. Near the Galapagos, upwelled water entrains iron rich volcanic sediments resulting in a phytoplankton bloom downwind of the Galapagos [*Feldman et al.*, 1984]. Careful study of high resolution bathymetry in comparison with ocean color data may yield other nutrient blooms associated as much with sediment and bathymetry as with current motions or wind.

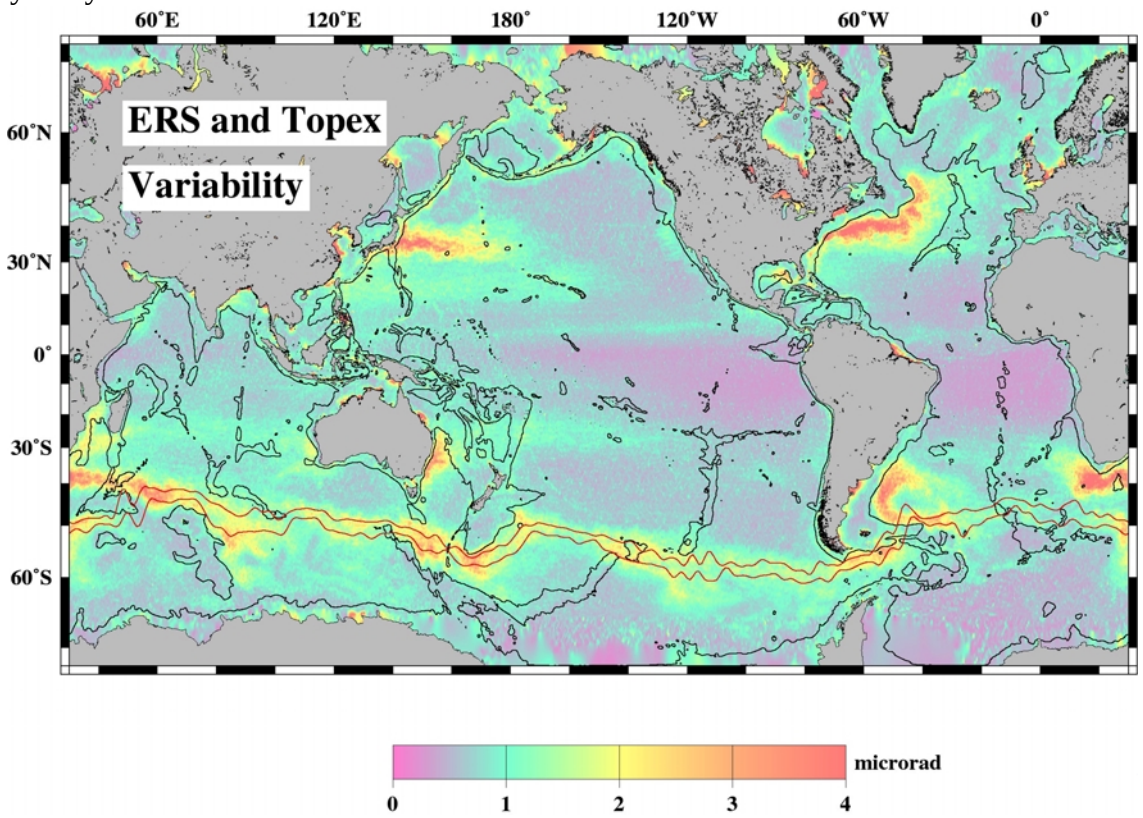

Figure 2.9 Mesoscale slope variability from Topex and ERS repeat-pass altimetry. Note regions of highest ocean variability are concentrated in ocean areas greater than 3000 m deep (contour lines). A comparison with Figure 2.8 also that, in the deep ocean, the highest variability occurs over smooth seafloor.

Finally, just as tidal dissipation may be linked with bottom roughness, mesoscale motions in the ocean may also be controlled by roughness. A preliminary study by *Gille et al.* [2000] compared bottom

roughness (Figure 2.8) with upper ocean mesoscale variability (Figure 2.9). Results showed that eddy kinetic energy (EKE) is greatest in the deeper ocean areas and over smooth seafloor. This anti-correlation between roughness and variability is strongest at higher latitudes suggesting a communication of the surface currents with the deep ocean floor in locations with low stratification. Rough bathymetry may transfer energy from the 100-300 km eddy length scales resolved by altimetry to smaller scales or to vertically propagating motions resulting in an apparent loss of EKE. Since numerical ocean models do not yet account for spatial variations in bottom friction and moreover, since they incorporate ad-hoc dissipation mechanisms, improvements in seafloor depth and roughness may ultimately lead to a better understanding of deep ocean mixing. The link between seafloor roughness and spreading rate provides an interesting possibility that vertical mixing of paleo-oceans depended on the average spreading rate of the ocean floor and thus the waxing and waning of the mantle convection patterns.

2.4 Structure of continental margins and exploration of offshore sedimentary basins

Continental Margins

All continental margins either were or are active plate boundaries. The transition from oceanic to continental crust is structurally complex and often obscured by thick layers of sediment shed from the continent. The various sedimentary layers and basement are of contrasting composition and density. Changes in the thickness and elevation of these layers can be tracked with gravity anomaly data. The continuous high-resolution data set of altimetric gravity anomalies that would be collected during a high resolution altimeter mission would dramatically improve our understanding of the variety of continental margins. These data would help complete understanding of the processes (plate tectonic and sedimentary) that create and modify these features over geologic time facilitating more accurate predictions of the location and extent of economically significant oil and gas fields.

Understanding of continental margins has come slowly, built from independent surveys pursued by many scientific organizations, governments and corporations over the past fifty years. Each of these surveys has focused on a particular segment of a continental margin with a particular purpose in mind; scientific, legal or commercial. While these data sets have built our understanding, the accumulation of data has not resulted in a complete or systematic characterization of continental margins worldwide. An altimetric gravity anomaly dataset, continuous along and across the submerged margins of the continents, would provide a means for systematic exploration and inter-comparison of the complex transition from continental to oceanic crust. A high-resolution altimeter mission would provide this dataset.

This comprehensive data set, a uniform survey of the continental margins, has not been obtained during previous altimetric missions, could not be collected from a ship and will not be collected by any of the geopotential satellite missions planned by either NASA or the ESA. Previous and future altimetric missions have and will collect relatively low*er* resolution data. *The increase in resolution with the new mission will greatly increase our ability to* image crustal scale structures of scientific and commercial interest. Shipboard surveys, which can collect high-resolution data, are expensive and particularly

difficult to execute in the shallow waters that would be sampled during a high-resolution altimeter survey.

The altimetric gravity anomaly data set will be unique and immensely valuable for science and exploration;

- A complete data set which will facilitate comparisons between continental margins.
- An exploration tool which will direct oil and gas exploration and permit extrapolation of known structures from well-surveyed areas.
- A uniform, high-resolution data set continuous from the deep ocean to the shallow shelf which will make it possible to follow fracture zones out of the ocean basin into antecedent continental structures, to define and compare segmentation of margins along strike and identify the position of the continent-ocean boundary. *Conversely the continuity of geological features on land can be traced on to the Continental Margin.*
- An image of the gravity field useful for the study of mass anomalies (eg sediment type and distribution) and isostatic compensation at continental margins.

Hydrocarbon exploration

More than 60% of the Earth's land and shallow marine areas are covered by > 2 km of sediments and sedimentary rocks, with the thickest accumulations on rifted continental margins. Sedimentary basins are the low-temperature chemical reactors that produce most of the hydrocarbon and mineral resources upon which modern civilization depends. The science and technology for the discovery and production of these resources will remain vital to the world's economy for at least the next several decades. Figure 2.10 shows (in green) the known major offshore basins around the world.

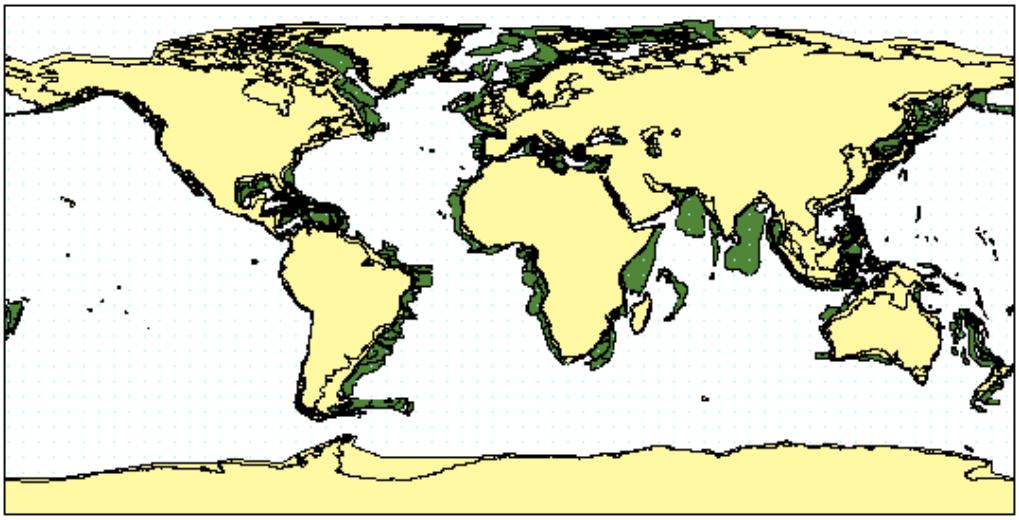

Figure 2.10 Major offshore sedimentary basins around the world (green)

Free-air marine gravity anomalies derived from satellite altimetry (Appendix B) are able to outline most of these major basins with remarkable precision. Figure 2.11 shows an image of the altimeter-

derived marine gravity field [*Sandwell & Smith*, 1997] on the northwestern shelf of Australia, and the outline of some of the major known offshore basins. There is clearly a general correspondence between the basins and the gravity anomalies.

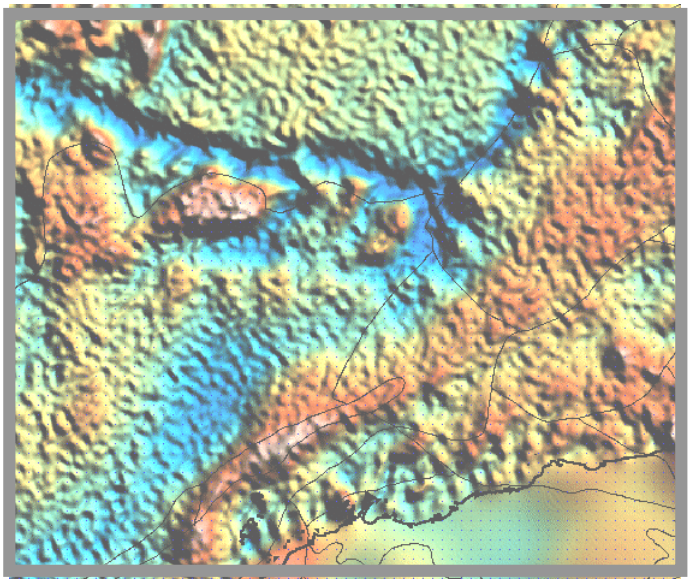

Figure 2.11 Major offshore-basin (Northwest Shelf of Australia) outlines superimposed on Free Air Gravity Anomaly Image

Gravity and bathymetry data derived from altimetry are also used to identify current and paleo submarine canyons, faults and local recent uplifts, active in modern time. These geomorphic features provide clues to where to look for large deposits of sediments. Figure 2.12 shows the paleo submarine canyons associated with the Indus (left, offshore Pakistan) and Ganges Rivers (offshore right, Bangladesh).

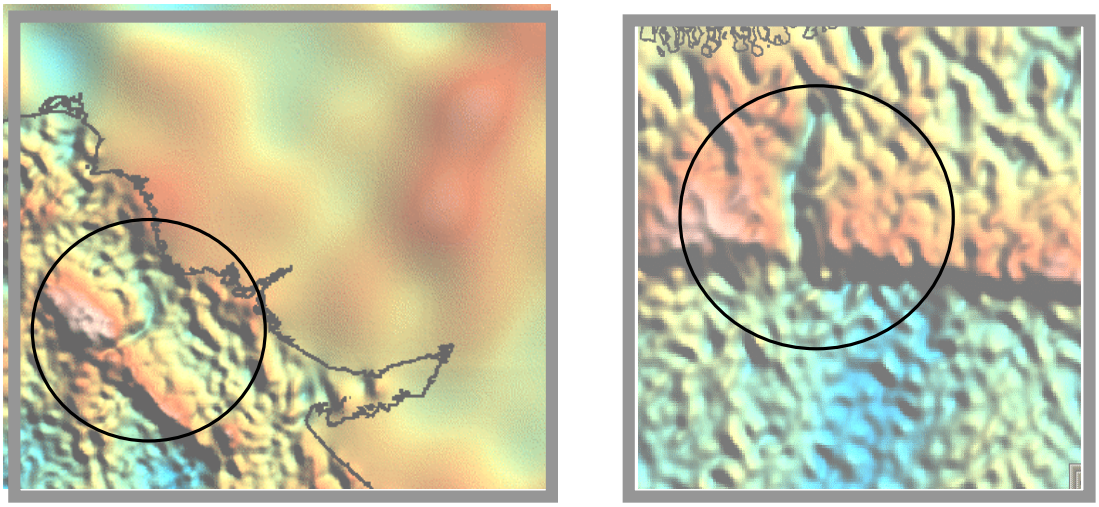

Figure 2.12 Submarine canyon associated with Indus River, Pakistan (left) Ganges River, Bangladesh (right).

While current altimeter data delineate the large offshore basins and major structures, they do not resolve some of the smaller geomorphic features and they cannot be used to detect some of the smaller basins (Table 2 and Figure 2.5). Wavelengths shorter than 40 km in the presently available data cannot be interpreted with confidence close to shore, as the raw altimeter data are often missing or unreliable near the coast. The exploration industry would like to have altimeter data with as much resolution as possible and extending as near-shore as possible. The 2-D seismic survey standard in the industry uses a track line spacing of 5 km, yielding structure maps with a 10 km Nyquist wavelength (Figure 2.13). Altimetry with a similar resolution is desirable.

Table 2. Wavelength and amplitude resolution required for typical geologic targets [Yale et al., 1998].

Target	Wavelength	Amplitude	
Buried cavities, tunnels, tanks	1 – 10 m	5-100 μGal	**not resolvable from space**
Pediment and seismic weathering layer thickness, shallow gas pockets, karst	10 – 200 m	0.05 mGal – 0.2 mGal	
Shallow salt domes and cap rock	200 – 1000 m	0.1 – 0.3 mGal	
Anticlines, faults deep salt, and overhang	500 – 4000 m	0.2 – 2.0 mGal	
Sedimentary basin structure. [Resolution commensurate with grid spacing (5-10 km) of seismic surveys for frontier basins.]	2 – 20 km	5 mGal	**new mission**
Sedimentary basin outlines and boundaries, plate tectonic structures	20 – 100 km	10 mGal	**current resolution Geosat and ERS**

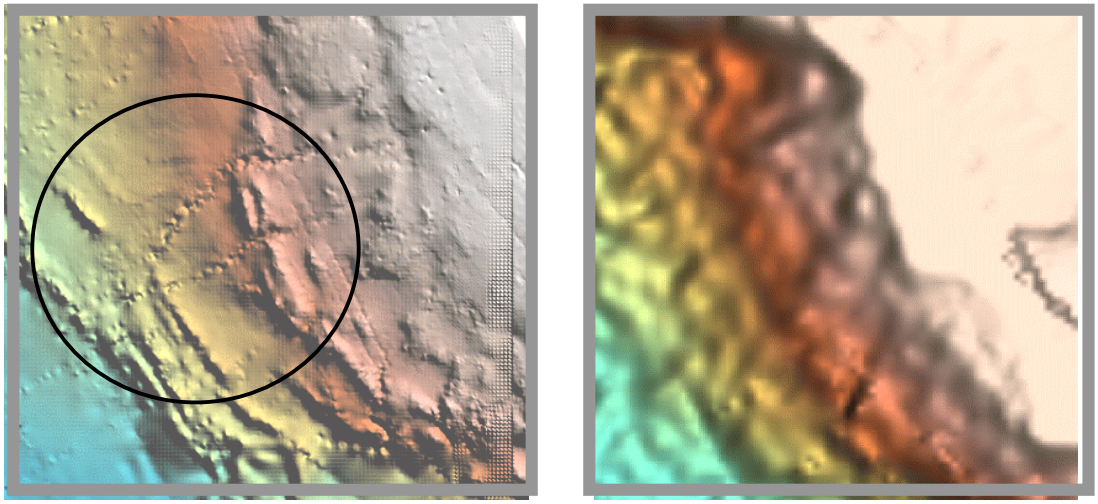

Figure 2.13 Left: Bathymetry obtained during 2-D seismic exploration survey. Right: Bathymetry derived from satellite altimetry. Although there is broad correspondence between the two, the finer features (surface expressions of some diapiric activity, incised canyons) are not interpretable from present altimetry.

3. LIMITATIONS OF PAST, CURRENT, AND PLANNED GRAVITY MISSIONS

There are three approaches to measuring marine gravity anomaly. Shipboard surveys provide the most direct approach. While older shipboard data have highly variable accuracy the newer, GPS-navigated surveys can achieve accuracy of better than 1 milligal [*Wessel and Watts*, 1988; *Yale et al*, 1998]. However, like bathymetric surveys, the marine coverage is sparse and inadequate for assessing the global roughness of the ocean floor or exploring the offshore sedimentary basins except in a few areas of active oil exploration such as the northern Gulf of Mexico. The second approach is to measure variations in gravitational acceleration at satellite altitude. Three new satellite gravity missions CHAMP [*Reiberger et al.*, 1996], GRACE [*Tapley et al.*, 1996], and GOCE [ref] will provide extremely accurate measurements of the global gravity field and its time variations [*Tapley and Kim*, 2001]. However, because these spacecraft measure gravity at altitudes higher than 250, they are unable to recover wavelengths shorter than about 160 km. As described in the preceding sections, we are primarily interested in wavelengths 15--100 km. Although these new missions offer little short-wavelength information, they provide the ideal reference field for shorter wavelength surveys. This greatly simplifies the design of a new satellite altimeter mission since long-wavelength accuracy will be is available.

The third approach to measuring marine gravity is satellite altimetry, in which a pulse-limited radar measures the altitude of the satellite above the closest sea surface point. The radar pulse reflects from an area of ocean surface (footprint) that grows with increasing sea state [see *Stewart*, 1985]. The superposition of the reflections from this larger area stabilizes the shape of the echo but it also smoothes the echo so that the timing of its leading edge less certain. By averaging many echoes (sampled at 1000 Hz) over multiple repeat cycles one can achieve a 10-20 mm range precision [*Noreus* 1995; *Yale et al.*,

1995]. Over a distance of 10 km (i.e. 1/2 wavelength) this corresponds to a sea surface slope error of 1-2 μrad which maps into a gravity error of about 1-2 mGal. There are several sources of error in these measurements but most occur over length scales greater than a few hundred kilometers [*Sandwell*, 1991; *Tapley et al.*, 1994; Appendix D]. For gravity field recovery and bathymetric estimation, the major error source is the roughness of the ocean surface due to ocean waves (Figures 3.1 and 3.2). Thus the only way to improve the resolution is to make many more measurements.

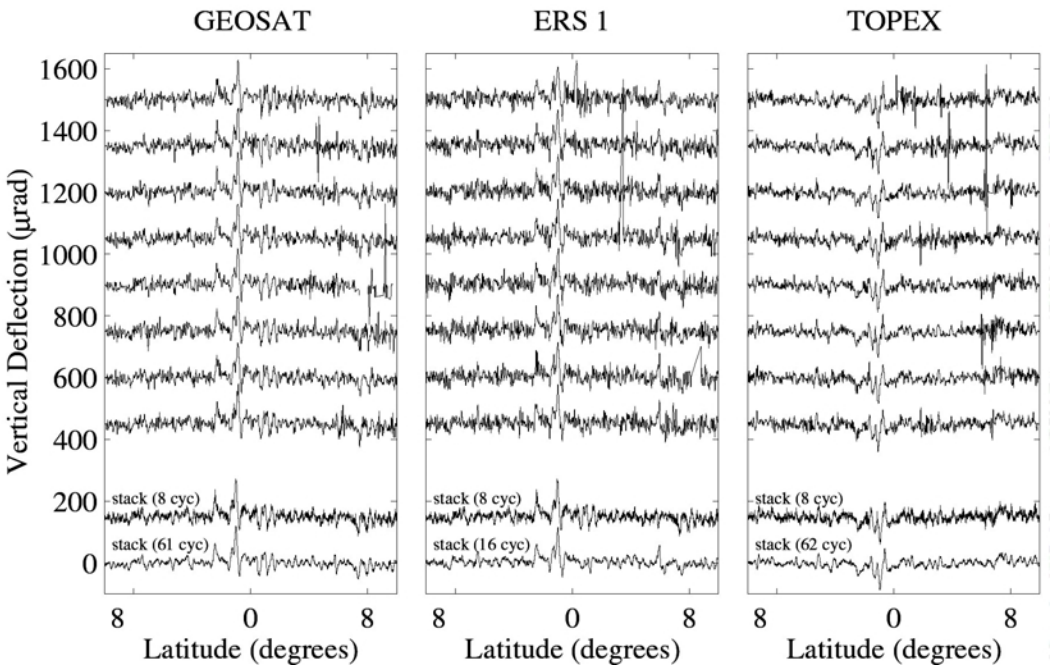

Figure 3.1 Profiles of sea surface slope along repeat tracks of Geosat, ERS1, and Topex [*Yale et al.*, 1995]. These tracks cross the Mid-Atlantic ridge in approximately the same location and provide large signals and relatively low, wave-height noise. Stacking reduces the noise in the along-track slope as the square root of the number of repeat profiles in the stack. This confirms that higher accuracy can be achieved by averaging. The rms deviation of the individual profiles with respect to the stacked profiles depends not only on the altimeter noise but also on the filters that are applied to the data prior to forming the geophysical data records (GDR). Thus a better measure of the data accuracy is provided by estimating the coherence between repeat tracks [see Figure 3.2].

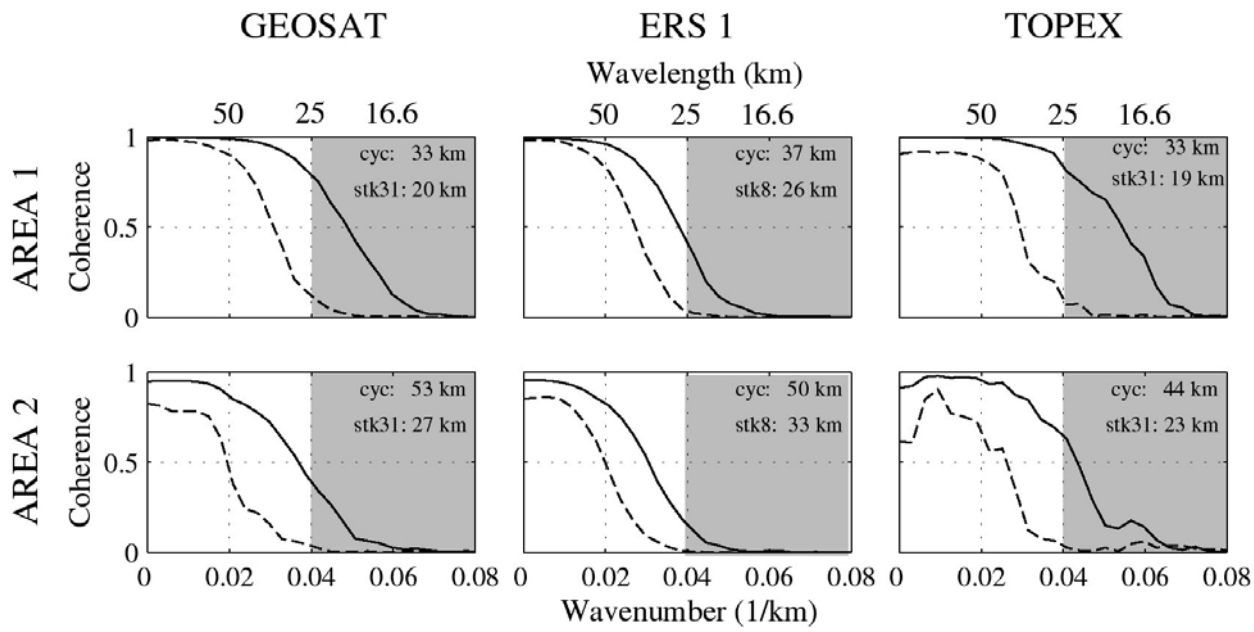

Figure 3.2 The along-track resolution of three radar altimeters Geosat, ERS1 and Topex, is assessed through cross-spectral analysis of repeat profiles [*Yale et al.*, 1995]. Two areas were selected for analysis. Area 1 over the equatorial Mid-Atlantic Ridge has a high signal due to the rugged seafloor and relatively low wave-height noise. Area 2 over the Pacific-Antarctic Ridge has a lower gravity signal but a much higher noise level because it is an area of large wave height. The two curves in each plot show coherence between individual cycles (dashed) and independent stacks (solid). The resolution estimates are at 0.5 coherence which represents a signal to noise ratio of 1.55. The resolution of the stacked profiles is better than the individual cycles. Topex and Geosat have generally better resolution than ERS1. The grey vertical box marks the resolution desired from a new altimeter mission. The range of desired resolution reflects the limiting factors of ocean depth and wave height.

Other sources of error include tide-model error, ocean variability, dynamic topography, ionospheric delay error, tropospheric delay error, and electomagnetic bias error. Corrections for many of these errors are supplied with the geophysical data record. However, for gravity field recovery and especially bathymetric prediction not all corrections are relevant or even useful. For example, corrections based on global models (i.e., wet troposphere, dry troposphere, ionosphere, and inverted barometer) typically do not have wavelength components shorter than 1000 km, and their amplitude variations are less than 1 m so they do not contribute more than 1 μrad of error. *Yale* [1997 and Appendix D] has examined the slope of the corrections supplied with the Topex/Poseidon GDR and found only the ocean tide correction [*Bettadpur and Eanes*, 1994] should be applied. The dual frequency altimeter aboard Topex/Poseidon satellite provides an estimate of the ionospheric correction, however, because it is based on the travel time difference between radar pulses at C-band and Ku-band, the noise in the difference measurement adds noise to the slope estimate for wavelengths less than about 100 km [*Imel*, 1994]. The most troublesome errors are associated with mesoscale variability and dynamic topography [*Rapp and Yi*, 1997]. The variability signal can be as large as 6 μrad [Figure 2.9] but fortunately it is confined to a few energetic areas of the oceans and given enough redundant slope estimates from nearby tracks [*Sandwell and Zhang*, 1989], some of this noise can be reduced by averaging. Dynamic topography typically has slopes of less than 0.1 μrad. However, along a few areas of steady intense western

boundary current, the slopes can be up to 6 μrad; this will corrupt both the gravity field recovery and the bathymetric prediction over length scales of 100-200 km.

An important remaining issue is the anisotropy in the accuracy of the current marine gravity fields derived from Geosat and ERS [*Sandwell and Smith,* 1997]. Note that the current Topex/Poseidon mission, in its 10-day repeat configuration, provides almost no additional gravity field information because of the wide ground track spacing (315 km). As shown in Figure 3.3 (lower panel), the E-W component of gravity field error at the equator is currently 3.5 times worse than the N-S error. There are two reasons for this. First, it has been shown that estimating sea surface slope by differencing heights on adjacent tracks results in slope estimates that are much less accurate than the along-track slope estimate [*Olgiati et al.,* 1995]. This is because the adjacent tracks, which are acquired at different times, have different environmental path delays and different orbit errors that cannot be entirely corrected with a crossover adjustment. In contrast, height measurements along the satellite tracks have common errors that are largely eliminated by computing the along-track slope. The second reason is simply that, at the equator, the Geosat and ERS tracks run mainly in the N-S direction. The situation is quite different at the turnover latitude of Geosat (72˚latitude), where the tracks are oriented in an E-W direction. The current Geosat/ERS configuration provides adequate control on the E-W slope for latitudes greater than about 60˚ latitude [Figure 3.3 - lower].

What is the optimal inclination for gravity field recovery given availability of the passed (Geosat/GM, ERS/GM) and planned (Cryosat) non-repreat radar altimeters? The upper panel in Figure 3.3 shows the area of ocean covered as a function of orbital inclination. Of course about 1/2 of the ocean area lies south of 30˚. The center panel shows the area-averaged degree of anisotropy as a function of orbital inclination for both prograde (solid) and retrograde (dashed). The optimal prograde inclination (Op) is 50˚ while the optimal retrograde (Or) is slightly higher 55˚ (125˚ inclination). Geosat and Topex inclinations provide about the same area-averaged inclination although a more detailed evaluation shows Topex tracks are more orthogonal in the low latitudes (< 20˚) where the current gravity fields suffer from poor E-W control. The International Space Station (ISS), which has a non-repeat orbit, is nearly optimal for this application. The east components shows greater improvement than the north component and the final error level after 6 years is 1 to 1.5 μrad. The desired noise level of about 1 μrad or 1 mGal can be achieved with a new if the mission duration exceeds about 6 years.

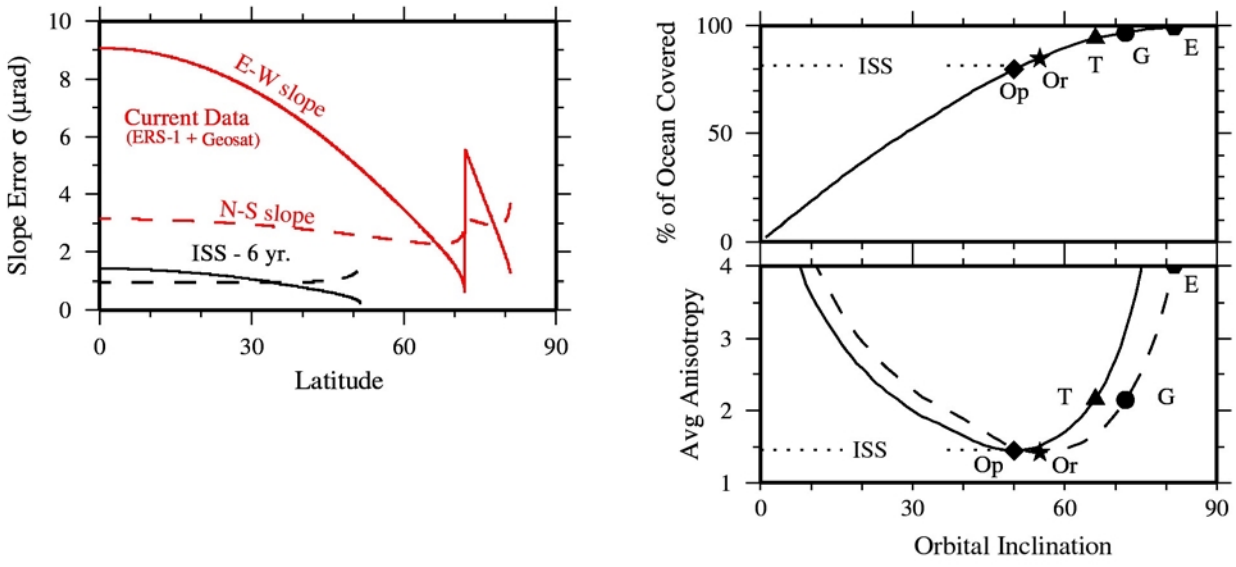

Figure 3.3 (left -red curves - Current) Propagation of along-track slope error from 1.5 years of dense Geosat coverage and 1 year of dense ERS-1 coverage into east (solid) and north (dashed) components of sea surface slope recovery versus latitude. At the equator, the Geosat and ERS tracks mainly run N-S so the N-S component is well determined (dashed red curve) while the E-W component of sea surface slope is poorly determined (solid red curve). The black curves show the improvement in E-W (solid) and N-S (dashed) slope error resulting from a new delay-doppler altimeter in an ISS (52˚) orbital inclination for 6 years. We assumed that the ERS-1 data have twice the noise level as the Geosat data and the new delay-doppler altimeter has one half the noise level of Geosat (Keith Raney, personal communication, 2001). Current error estimates in μrad are based on comparisons with shipboard gravity profiles [*Marks*, 1996; *Sandwell and Smith*, 1997]; typical errors are 3-5 μrad.
(right) Trade-off analysis to establish the average N-S to E-W anisotropy as a function of orbital inclination (solid – prograde, dashed – retrograde). The optimal inclinations are 50˚ (Op) and 55˚ (Or), respectively. The ERS (E), Geosat (G) and Topex (T) inclinations are good at higher latitudes but suffer from poor E-W slope recovery at low latitudes where the area of ocean (right-upper) is maximum.

The final issue in gravity field recovery from the Geosat and ERS altimeters is related to the coastal data (Figure 3.4A). The issues for Geosat and ERS are different but both are illustrated in Figure 3.4B showing the available ground tracks in the Caspian Sea. The ERS-1 geodetic mission data are absent in this inland sea because the altimeter was switched to the ice mode where the ranging resolution is optimized for land or ice topography but inadequate for gravity field recovery. Many of the Geosat tracks over this sea are short or absent because the Geosat altimeter sometimes had trouble re-acquiring the sea surface when transitioning from land to water. Figure 3.4C and 3.4D shows the track density that would be acquired in 1.5 years for a satellite in a Topex and ISS inclination, respectively and with perfect ocean tracking. The differences are significant and in this particular area, just 1.5 years of non-repeat coverage would provide a factor of 2 improvement in accuracy.

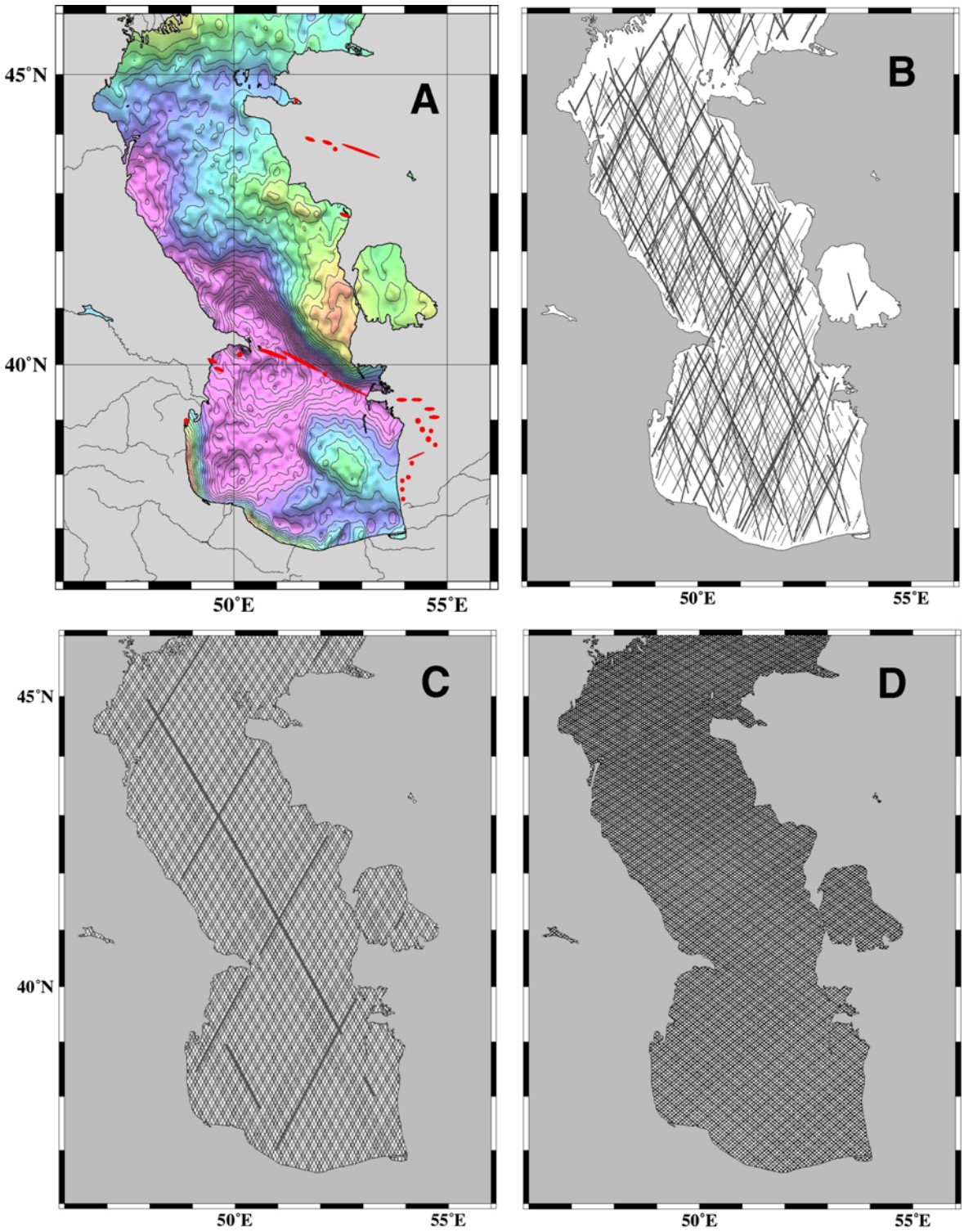

Figure 3.4 (A) Gravity anomaly of the Caspian Sea (10 mGal contour interval) derived from all available satellite altimeter data (Geosat, ERS and Topex). Major oil fields are sketched in red. Future exploration will focus on the northern Caspian near the outlet of the Volga River. (B) Tracks of available altimeter data show less-than-optimal coverage because ERS data are not available (land mask) and many Geosat profiles are missing due to problems with the onboard tracker re-acquiring the water surface. (C) Tracks from 1.5 years of a new satellite altimeter in a Topex-inclination orbit and assuming full data recovery up to the coastlines. (D) Tracks from 1.5 years of a new satellite altimeter in an ISS orbital inclination.

4. BASELINE MISSION REQUIREMENTS

How should a new ocean mapping mission be designed? What could it resolve?

In section 2.2 we have seen that understanding tidal dissipation and ocean mixing may ultimately require sea floor roughness on very short spatial scales, even those too short to be measured by altimetry. However, as section 2.1 has shown (Figure 2.4), the roughness at these scales is well-modeled by a self-affine surface, so that the seafloor topography may be characterized statistically at wavelengths which are shorter than the corner wavenumber [*Goff and Jordan*, 1988]. Thus if one could map the oceans with enough resolution to establish the total power and the corner wavenumber, the statistical properties of the shorter part of the spectrum would follow from the self-affinity.

The corner wavenumber for the two patches we have examined (MAR and EPR) are both 20 km. However, it should be noted that other major complications on the seafloor such as fracture zones and seamounts can change both the total power and corner wavenumber. Moreover, the spectrum of the seafloor is usually anisotropic with fracture zones oriented parallel to the spreading direction and abyssal hills perpendicular to the spreading direction. The important point is that if one could map the full topography of the ocean floor to better than a 20 km wavelength, one could extrapolate the full anisotropic roughness spectrum; the anisotropy is important because deep tidal currents interact with the bottom only along their direction of flow. Current bathymetric prediction can capture wavelengths of only 40 km on smooth seafloor and about 25 km on rough seafloor. A new mission with sufficient accuracy to recover 15-km wavelengths would capture essentially all the interesting geophysics of the seafloor spreading process, and in addition, the statistical properties of the finer-scale roughness.

To achieve significant contributions in several areas of geophysics, physical oceanography, and climate research, an altimeter mission having the following characteristics is needed:

- ***Altimeter Precision*** - The most important requirement of this new mission is improvements in ranging technology to achieve a factor of 2 improvement in range precision (with respect to Geosat and Topex) in a typical sea state of 3 m. In shallow water, where upward continuation is minor, and in calm seas where waves are not significant (e.g. Caspian Sea), it will also be important to have an along-track footprint that is less than 1/4 of the resolvable wavelength of about 10 km. This footprint is smaller than the standard pulse-limited footprint of Geosat or Topex .
- ***Mission Duration*** - The Geosat Geodetic Mission (1.5 years) provides a single mapping of the oceans at ~5 km track spacing. Since the measurement noise scales as the square root of the number of measurements, a 6-year mission will reduce the error by a factor of 2. This combined with the factor of 2 gain by improved instrumentation results in an overall factor of 4 improvement.
- ***Moderate inclination*** - Current non-repeat orbit altimeters have high inclination (72˚ Geosat, 82˚ ERS) and thus poor accuracy of the E-W slope at the equator. The new mission should have an inclination between 50˚ and 65˚ degrees to improve E-W slope recovery (Figure 3.3)
- ***Near-shore tracking*** For applications near coastlines, the ability of the instrument to track the ocean surface close to shore, and acquire the surface soon after leaving land, is desirable (Figure 3.4).

Finally, it should be stressed that the basic measurement is not the height of the ocean surface but the slope of the ocean surface (Appendix B). The height differences over horizontal distances from a few km to a few hundred km must be measured with sufficient accuracy and precision that the horizontal slope of the sea surface along the satellite track can be calculated with a precision of about 1 microradian (10 mm height change over 10 km horizontal distance). The band of wavelengths we need to resolve is from 8 to a few hundred km (full wavelength). This requires careful processing of the radar pulse data at high sampling rates.

The need to resolve height differences, and not heights, means that the mission can be much cheaper than other altimeter missions and can take advantage of spacecraft platforms which are less stable than other missions require. This is because the absolute height, and any component of height which changes only over wavelengths much longer than a few hundred km, is irrelevant, as it contributes negligible slope (Table 3). Therefore one can tolerate large spacecraft motions, and errors modeling them, so long as they vary slowly with distance. Also, one need not measure the radar propagation delays in the ionosphere and troposphere, as the slopes of these corrections are also negligible (Table 3 and Appendix D).

Table 3 Signal and Maximum Error in Sea Surface Slope

Signal or Error source	**Length (km)**	**Height (cm)**	**Slope (μrad)**	**Mission-avg. slope (μrad)**
Gravity Signal	12–400	1–300	1–300	1–300
Measurement error sources:				
Orbit errors[1]	8000–20,000	400–1000	< 0.5	< 0.2
Ionosphere[2,3]	> 900	20	< 0.22	< 0.1
Wet Troposphere[4]	> 100	3-6	< 0.6	< 0.3
Oceanographic error sources:				
Basin-scale circulation (steady)[5]	> 1000	100	< 1	< 1
El Niño[6], inter-annual variability, planetary waves	> 1000	20	< 0.2	< 0.1
Deep ocean tide model errors[4]	> 1000	3	< 0.03	< 0.01
Coastal tide model errors[3,6]	50–100	< 13	< 2.6	< 1.1
Eddys & Mesoscale Variability[7]	60–200	30–50	2.5–5	1–2
Meandering jet (Gulf Stream)[5,8]	100–300	30–100	3–10	2–4
Steady Jet (Florida Current)[5,8]	100	50–100	5–10	5–10

[1]Dynamic orbit determination using the ISS SIGI system, considering errors in force, measurement, attitude, center of mass, and effect of EXPRESS nadir pallet moment arm. [2]Imel [1994]. [3]Yale [1997]. [4]Chelton et al. [2001]. [5]Fu & Chelton [2001]. [6]Picaut & Busalacchi [2001]. [6]Shum et al. [2001]. [7]LeTraon & Morrow [2001]. [8]Smith & Sandwell [1995].

Appendix A. Popular articles triggered by the declassification of geosat altimetry

Magazine Articles

Carrol-Strait, G. (1996, May, 1996). Beneath the Feet of Neptune. ***The World & I*** p. 158-165.

Kunzig, R. (1996, March, 1996). The Seafloor from Space. ***Discover*** p. 58-64.

Lawler, A. (1995, November 1995). Sea-Floor Data Flow from Postwar Era. ***Science,*** p. 727.

McNutt, M. (25 January, 1996). The 5-billion-dollar bumps, ***Nature.***

Monastersky, R. (1995, 16 December, 1995). A New View of the Earth. ***Science News*** p. 410-411.

Reichhardt, T. (1996, 28 May, 1996). Water World. ***Popular Science*** p. 70-71.

Small, C., & Sandwell, D. (1996, March, 1996). Sights Unseen. ***Natural History*** p. 28-33.

Yulsman, T. (1996, June, 1996). The Seafloor Laid Bare. ***Earth*** p. 42-51.

Newspaper Articles

Anonymous (25 October, 1995). Military Data Helps Detail Ocean Map. ***Sudbury Times***

Anonymous (November, 1995). New Seafloor Map Released by NOAA, Scripps. ***Sea Technology***

Anonymous (24 October, 1995). Scientists make detailed ocean map. ***Daily Republic***

Bokstede, H. (26 January, 1996). Under ytan lurar berg och dalar. ***Svenska Dagbladet***

Boyd, R. (24 October, 1995). A detailed map of the entire ocean floor. ***Philadelphia Inquirer***

Boyd, R. (24 October, 1995). Mapping secrets of the deep. ***Press-Telegram***

Boyd, R. (24 October, 1995). Once-secret photos help map the oceans. ***Sun News***

Boyd, R. (24 October, 1995). A road map to the ocean floor. ***Miami Herald***

Boyd, R. (24 October, 1995). Satellite data helps scientists create map of ocean floor. ***San Jose Mercury News***

Boyd, R. (24 October, 1995). Satellite map of ocean floor offers detailed 'data feast'. ***News Tribune***

Boyd, R. (24 October, 1995). Scientist's full-color satellite maps shine light on ocean floor. ***Los Angeles Times***

Boyd, R. (24 October, 1995). Scientists create detailed map of ocean floor. ***Detroit Free Press***

Boyd, R. (24 October, 1995). Spectacular Views of Earth's Oceans. ***Duluth News-Tribune***

Broad, W. (24 October, 1995). Map Makes Ocean Floors as Knowable as Venus. ***The New York Times***

Broad, W. (25 October, 1995). Map of Ocean Floor Opens a Window on the Mysteries of the Sea. ***International Herald Tribune***

Broad, W. (24 October, 1995). New map of ocean floors provides glimpse of sunless depths. ***Ottawa Citizen***

Carlowicz, M. (31 October, 1995). New Map of Seafloor Mirrors Surface. ***EOS, Transactions, AGU,*** p. 441-442.

Hill, R. (22 November 1995). Deep Details. ***Oregonian,*** p. A16.

Ladbury, R. (September 1995). Satellite Mapping of Terra Incognita Provides Welcome Relief. ***Physics Today***

Lane, E. (24 October, 1995). Bottom of Sea Viewed in Detail. ***Newsday***

Lane, E. (24 October, 1995). Detailed new map made by satellite shows ocean floor. ***Seattle Times***

Miller, K. (24 October, 1995). Spy data brings ocean floor to light. ***USA Today***

Miller, K. (24 October, 1995). Spy satellite data provide clear view of ocean floor. ***Courier-Post***

Miller, K. (24 October, 1995). Spy Satellite Info Helps Scientists Map Ocean Floor. ***Chicago Sun-Times***

Morgan, N. (October 12, 1995). Scripps team roams oceans with space maps. ***The San Diego Union Tribune***

Associated Press (25 October, 1995). Map provides new details about ocean floor. ***Daily Herald***

Associated Press (24 October, 1995). Scientists make first detailed map of ocean floor. ***Washington Times***

Associated Press (29 October, 1995). Using satellite 'data feast,' detailed pictures of ocean floors emerge. ***Chicago Tribune***

Schmid, R. (8 November, 1995). Declassified Data Reveals New Views of Ocean Bottom. ***Washington Post***

Schmid, R. (21 November, 1995). Satellites help scientists map ocean floor. ***Capper's***

Schmid, R. (24 October, 1995). Scientists Map Ocean Floor with Declassified Spy Sat. Data. ***Washington Post,***

P-I. News Service (24 October, 1995). Map opens new avenues on the ocean floor. ***Seattle Post-Intelligencer***

Snavely, R. (November, 1995) Declassified Navy Data Helps SIO Map Ocean. ***The Guardian***

Spotts, P. (25 October, 1995). Seabed Exposed in Unparalled Detail. ***Christain Science Monitor***

Appendix B. Geoid height, vertical deflection, and gravity anomaly

The geoid height $N(\mathbf{x})$ and other measurable quantities such as gravity anomaly $g(\mathbf{x})$ are related to the anomalous gravitational potential $V(\mathbf{x},z)$ [*Heiskanen and Moritz*, 1967]. Since we are primarily interested in short wavelength anomalies, we assume that all of these quantities are deviations from a spherical harmonic reference earth model [e.g., EGM96, *Lemoine et al.*, 1998] so that a planar approximation can be used for the gravity computation. In the following equations, the bold $\mathbf{x}$ denotes the coordinate (x,y) in the horizontal plane.

To a first approximation, the geoid height is related to a potential by Bruns' formula,

$$N(\mathbf{x}) \cong \frac{1}{g_0} V(\mathbf{x},0) \ , \tag{1}$$

where g_o is the latitude-dependent acceleration of normal gravity at sea level (~9.8 m s^{-2}). The gravity anomaly at sea level is the vertical derivative of the potential,

$$g(\mathbf{x}) = -\frac{\partial V(\mathbf{x},z)}{\partial z}\bigg|_{z=0} \ ; \tag{2}$$

while the east component and north component of vertical deflection are the slope of the geoid in the x and y-directions, respectively

$$\eta(\mathbf{x}) = \frac{-1}{g_0}\frac{\partial V(\mathbf{x},z)}{\partial x}\bigg|_{z=0}, \quad \xi(\mathbf{x}) = \frac{-1}{g_0}\frac{\partial V(\mathbf{x},z)}{\partial y}\bigg|_{z=0} \ . \tag{3}$$

These quantities are related to one another through Laplace's equation,

$$\frac{\partial^2 V}{\partial x^2} + \frac{\partial^2 V}{\partial y^2} + \frac{\partial^2 V}{\partial z^2} = 0 \ . \tag{4}$$

Following *Haxby et al.* [1983] the differential equation (4) is reduced to an algebraic equation by Fourier transformation

$$\hat{g}(\mathbf{k}) = \frac{i g_0}{|\mathbf{k}|}\left[k_x \hat{\eta}(\mathbf{k}) + k_y \hat{\xi}(\mathbf{k})\right] , \tag{5}$$

in which we have used the Fourier wavevector $\mathbf{k} = (k_x, k_y)$ with wavenumbers $k_x = 2\pi/\lambda_x$ and $k_y = 2\pi/\lambda_y$ measured in radians per length, λ being the wavelength, so that the Fourier transforms are

$$\hat{f}(\mathbf{k}) = \iint f(\mathbf{x}) \exp[-i\mathbf{k} \bullet \mathbf{x}] \; dx \, dy \; ,$$

$$f(\mathbf{x}) = \frac{1}{4\pi^2} \iint \hat{f}(\mathbf{k}) \exp[i\mathbf{k} \bullet \mathbf{x}] \; dk_x \, dk_y \; . \qquad (6)$$

To compute gravity anomaly from a dense network of satellite altimeter profiles of geoid height, one constructs grids of east η and north ξ vertical deflection. The grids are then Fourier transformed and Eq. (5) is used to compute gravity anomaly [*Haxby et al.*, 1983; *Sandwell,* 1992]. At this point one can add the long wavelength gravity field from the spherical harmonic model to the gridded gravity values in order to recover the total field; the resulting sum may be compared with gravity measurements made on board ships (Figure A1). A more complete description of gravity field recovery from satellite altimetry can be found in *Hwang and Parsons* [1996], *Sandwell and Smith* [1997], and *Rapp and Yi* [1997].

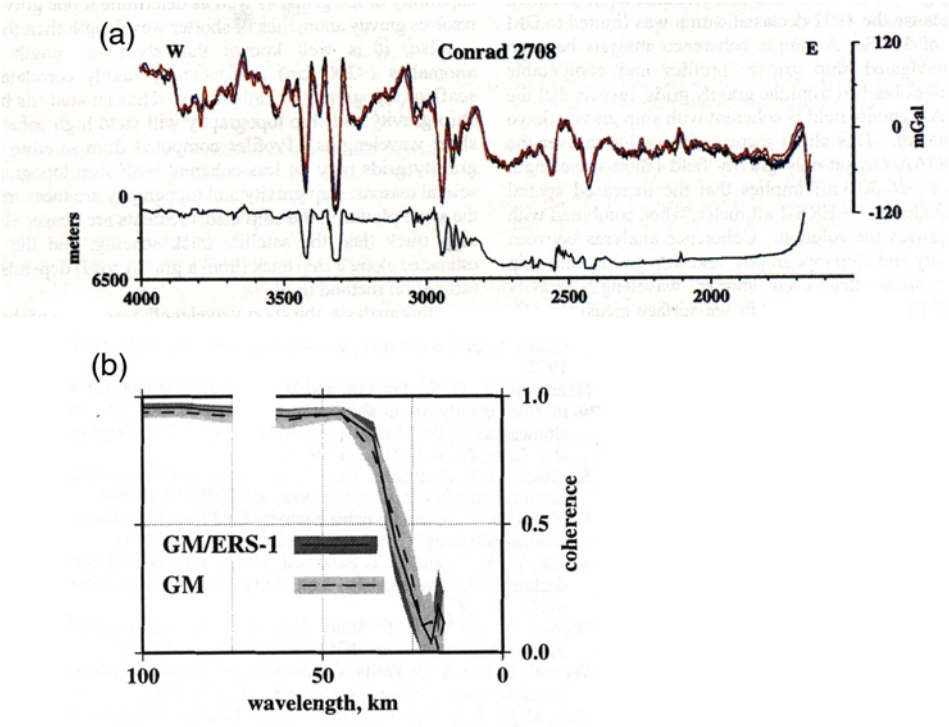

Figure A1 Comparison between free-air gravity anomaly recovered from satellite altimetry and shipboard gravity profile [*Marks,* 1996]. (a) The rms difference between the satellite and ship gravity for two different satellite gravity analyses (SIO and NOAA) is 8.7 and 9.3 mGal, respectively. The coherence between satellite and ship gravity is high for wavelengths greater than 50 km and falls to a value of 0.5 at 29 km wavelength. This E-W profile at low latitude represents a worst-case satellite gravity recovery (see Figure 3.3).

The important issue for bathymetric estimation is revealed by a simplified version of Eq. (5). Consider the sea surface slope and gravity anomaly across a two-dimensional structure which depends

on x but not y. The y-component of slope is zero so conversion from sea surface slope to gravity anomaly is simply a Hilbert transform:

$$\hat{g}(k) = ig_0 \,\mathrm{sgn}(k_x)\,\hat{\eta}(k). \qquad (7)$$

Now it is clear that one μrad of sea surface slope maps into 0.98 mGal of gravity anomaly and similarly one μrad of slope error will map into ~1 mGal of gravity anomaly error. Thus the accuracy of the gravity field recovery is controlled by the accuracy of the sea surface slope measurement. Since bathymetry is related to the short-wavelength portion of the field only (Appendix C), the accuracy of bathymetry predicted from gravity is especially sensitive to the errors in the short-wavelength slope estimates.

Appendix C. Sea surface gravity related to seafloor topography and sub-seafloor structure; bathymetric prediction.

Geologic processes generate topography on the ocean floor and lateral density variations below the sea floor at a variety of spatial scales. This topography and structure can produce small (parts in 10^6 to 10^4) anomalies in the magnitude (1 to 400 milliGals) and direction (1 to 400 μrad) of Earth's gravity field at the sea surface. These anomalies are manifest as geoid undulations in ocean surface topography measured by satellite altimetry, as described in Appendix B.

Correlation between seafloor topography (or subseafloor structure) and sea surface gravity anomalies is expected only over a limited wavelength band because of a number of factors. 1) The gravity to topography ratio (transfer function) becomes singular at both short wavelengths ($\lambda << 2\pi$ times mean ocean depth) and long wavelengths ($\lambda >>$ depth of compensation or flexural wavelength) due to upward continuation and isostatic compensation, respectively. 2) The short wavelength portion of the gravity to topography transfer function depends on well known parameters (ocean depth, crustal density), the longer wavelength portion is highly dependent on the elastic thickness of the lithosphere and/or crustal thickness. 3) Sediments raining down onto the seafloor preferentially fill bathymetric lows and can eventually completely bury the pre-existing basement topography. This adds a spatially-dependent and non-linear aspect to the gravity-to-topography transfer function. 4) The transfer function is three-dimensional although usually it is assumed to be isotropic in azimuth. Thus complete ocean surface gravity coverage from altimetry is required for bathymetric prediction. 5) Finally, in areas where the amplitude of the topographic relief approaches the mean depth, the transfer function is inherently non-linear [*Parker,* 1973]. Many previous studies have identified and addressed some of these issues [*Dixon et al.,* 1983; *Baudry and Calmant,* 1991; *Jung and Vogt,* 1992; *Smith and Sandwell,* 1994; *Sichoix and Bonneville,* 1996]. This appendix reviews these relationships. The amplitudes and wavelengths of the structures of interest here are small compared with the radius of the Earth, and so the planar approximation is used here as in Appendix B; quantities are functions of position in the horizontal plane,

and the same Fourier transform convention is used. For simplicity, the notation k will be used to indicate the scalar magnitude of the Fourier wavevector; $k = |\mathbf{k}|$.

The forward problem: Computing the gravity anomaly at sea level due to a given subsurface structure or sea floor topography

The relationship between gravity fields and their sources is linear in density, so that superposition may be used to describe the field as the sum of a number of elementary structures. The simplest description of structure is one in which an undulating interface separates regions of two different, but constant, densities (Figure C1). If the topography of the interface, measured positive upwards, is $h(\mathbf{x})$, if the plane $h(\mathbf{x}) = 0$ lies at a depth d below sea level, if the densities are ρ_1 above h and ρ_2 below h, and if the interface does not rise above sea level, then g, the gravity anomaly at sea level due to this structure is [*Parker,* 1973]

$$\hat{g}(\mathbf{k}) = 2\pi G\left(\rho_2 - \rho_1\right)\exp[-kd]\sum_{n=1}^{\infty}\frac{k^{(n-1)}}{n!}\Im\left\{\left[h(\mathbf{x})\right]^n\right\}, \qquad \text{(C1)}$$

where G is the Newtonian gravitational constant $6.6732\text{x}10^{-11}$ Nt-m^2/kg^2 and $F\{\}$ is the fourier transformation. The sum on the right hand side of equation (C1) is in the form of the Fourier transform of a Taylor series expansion. This comes from using the power series for $\exp[kh]$, and the sum converges rapidly when kh is small, which is to say, h is smooth, or $2\pi h/\lambda$ is small for the largest magnitude of h and every wavelength λ in the spectrum of h. Note that one is free to adjust the value of d (the depth of the plane $h = 0$) so as to minimize the maximum magnitude of h. Also, at short wavelengths, where $\lambda \sim< 2\pi d$, any errors made in truncating the sum will be strongly attenuated by the factor $\exp[-kd]$; thus the convergence of the series is not a serious issue if the maximum magnitude of h is much less than d.

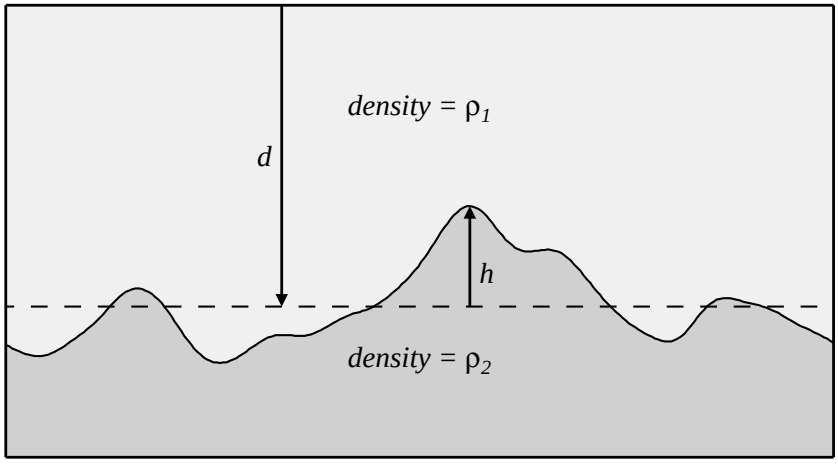

Figure C1. Topography on the interface between two layers of constant density gives rise to a gravity anomaly. This description can be applied both to ocean floor topography and to the sub-seafloor structures within sedimentary basins.

In practice it is often adequate to use only the first term in the sum in (C1), which yields the approximation

$$\hat{g}(\mathbf{k}) = 2\pi G\left(\rho_2 - \rho_1\right) \exp[-kd]\, \hat{h}(\mathbf{k}) \ , \qquad \text{(C2)}$$

which has the convenient form

$$\hat{g}(\mathbf{k}) = f(k)\, \hat{h}(\mathbf{k}) \ , \qquad \text{(C3)}$$

representing an isotropic, spatially invariant, linear system with *h* as input and *g* as output. It is isotropic because the relationship depends on *k* and not **k**. It is spatially invariant because the relationship $f(k)$ between $h(\mathbf{x})$ and $g(\mathbf{x})$ is independent of **x**. In this form, the relationship between gravity anomalies and their causative structure may be reduced to a simple linear operator, or filter, facilitating analysis. In a region so large as to combine a variety of heterogeneous geologic processes, the relationship between gravity and structure cannot be so simply described, as the density and other parameters may not be spatially invariant across different geologic settings. However, the linear filter description is a useful first-order description of elementary structures at small spatial scales, which are of interest in this paper.

Note that the strength of the gravity anomaly is proportional to the product of the density contrast across the interface, $\left(\rho_2 - \rho_1\right)$, and the amplitude of the interface, *h*. The constant term in (C2), $2\pi G\left(\rho_2 - \rho_1\right)$, is sometimes called the "Bouguer constant" after the formula for the gravity due to a horizontal slab of material (Bouguer, 1749; Turcotte and Schubert, 1982, section 5.7). In what follows we will be primarily concerned with the estimation of thinly sedimented ocean floor topography from gravity, and so we will take $\rho_1 = \rho_w$, the density of sea water, and $\rho_2 = \rho_h$, the density of oceanic crust; however, the equations also apply to the situation where *h* is an interface between strata in a sedimentary basin, or between sedimentary rocks and basement rocks. For seafloor topography, with ρ_h = 2800 kg/m^3 and ρ_w = 1030 kg/m^3, the Bouguer constant is approximately 75 mGal per km of topography.

Upward continuation

The factor $\exp[-kd]$ in (C2) accomplishes an operation known as "upward continuation". In upward continuation through a distance *d*, any constituent of the gravity field with characteristic horizontal scales λ_x, λ_y is attenuated by an amount $\exp[-2\pi d/\lambda]$, where $\lambda^{-1} = \sqrt{\lambda_x^{-2} + \lambda_y^{-2}}$. Shorter wavelengths are more strongly attenuated than longer ones, and if an object is elongated, the attenuation depends more strongly on the shorter of its two characteristic wavelengths λ_x, λ_y. Topography with a wavelength of $\lambda = 2\pi d$ will have its gravity effect attenuated by an amount $1/e \cong 0.37$; if *d* = 4 km this wavelength is about 25 km, and if *d* increases with sea floor age (e.g., Parsons and Sclater, 1977), then the 1/*e* wavelength will be greater than 20 km for all ages greater than about 2 Ma. This attenuation due

to water depth is one of the factors limiting the resolution of sub-surface structures by sea surface gravity data.

Isostatic compensation

A long history of geophysical investigations (reviewed in Heiskanen and Vening Meinesz, 1958) has shown that large scale topographic features on the Earth are isostatically compensated. Studies of isostasy in the oceans have found that a "flexural isostatic model" usually characterizes the relationship between *g* and *h*. Flexural isostasy is a generalization of an isostatic model given by Airy (1855). In Airy's model the topography floats on the mantle; the flexural model adds a term representing the mechanical strength of the lithosphere to the buoyant support Airy proposed. Flexure was proposed by Barrell (1914), applied to pendulum gravity measurements in the ocean by Vening Meinesz (1941), and refined by Gunn (1943) and Walcott (1970, 1976). Dorman and Lewis (1970) and Banks et al. (1977) developed the linear system approach to isostasy, and Mackenzie and Bowin (1976), Watts (1978, 1979), McNutt (1979), Watts et al. (1980) and then many others investigated flexure of the ocean lithosphere. Watts (1983) gives a review.

In the Airy model, the mass excess represented by positive topography *h* is balanced by a mass deficit caused by negative (downward) displacements of the Mohorovicic discontinuity (moho). If *w* measures the displacement of the moho from where it would be if *h* were zero, then balancing the deviatoric vertical normal stresses σ_{zz} caused by *h* and *w* leads to

$$(\rho_h - \rho_w)\gamma h + (\rho_m - \rho_h)\gamma w = 0 \ , \qquad \text{(C4)}$$

where ρ_m is the density of the mantle beneath the moho and γ is the total acceleration of normal gravity, from which it follows that

$$w = -\left[\frac{(\rho_h - \rho_w)}{(\rho_m - \rho_h)}\right] h \ . \qquad \text{(C5)}$$

If we apply the approximation (C2) twice to calculate the combined gravity effects of *h* and *w*, with *w* given from *h* by (C5), we obtain an equation of the form (C3) with

$$f(k) = 2\pi G(\rho_h - \rho_w)\exp[-kd]\{1 - \exp[-kc]\} \ , \qquad \text{(C6)}$$

where *c* is the distance between the $h = 0$ and $w = 0$ planes, that is, the mean crustal thickness. Now in addition to the upward continuation effect of (C2) we also have attenuation of long wavelengths (long with respect to *c*) due to the last term in (C6). In this case *g* is non-zero only in a band of wavelengths longer than a few times *d* and shorter than a few times $d + c$.

Flexural isostasy adds to equation (C4) an additional deviatoric stress σ_{zz} term representing the lithosphere's resistance to being deformed into the shape *w*. The resistance is characterized by a parameter *D* called the "flexural rigidity". The stress balance becomes

$$(\rho_h - \rho_w)\gamma h + (\rho_m - \rho_h)\gamma w + D\nabla^4 w = 0 \qquad \text{(C7)}$$

in which ∇^4 is the biharmonic operator. (Some authors generalize (C7) to include spatially-varying *D* or the effect of material of another density filling flexural depressions, but these generalizations prevent the use of the Fourier transform to obtain a spatially-invariant linear system.) By employing Fourier transforms one finds that

$$\hat{w}(\mathbf{k}) = -\left[\frac{(\rho_h - \rho_w)}{(\rho_m - \rho_h)}\right]\Phi(k)\,\hat{h}(\mathbf{k}) \qquad \text{(C8)}$$

where

$$\Phi(k) = \left[\frac{1}{\left(1 + (\lambda_f k)^4\right)}\right] \qquad \text{(C9)}$$

is a "flexural isostatic filter" with a wavelength of half-amplitude

$$\lambda_f = 2\pi\left[\frac{D}{\gamma(\rho_m - \rho_h)}\right]^{1/4} \qquad \text{(C10)}$$

called the "flexural wavelength". Other definitions in the literature absorb various constant factors into λ_f. Using (C8) instead of (C5) and proceeding as before, one obtains a relationship in the form (C3) with

$$f(k) = 2\pi G(\rho_h - \rho_w)\exp[-kd]\{1 - \exp[-kc]\Phi(k)\}\ . \qquad \text{(C11)}$$

One may view Airy isostasy as a special case of flexural isostasy, for when $D = 0$ the flexure equations reduce to the Airy equations. In the literature, further generalizations of (C11) are obtained by assuming that the oceanic crust has two or more layers, each of which has constant thickness and density and flexes into the same shape *w* under the load *h* (Watts, 1978; Ribe and Watts, 1982; Müller and Smith, 1993). Under these assumptions one obtains an $f(k)$ with values very similar to those of the simpler (C11).

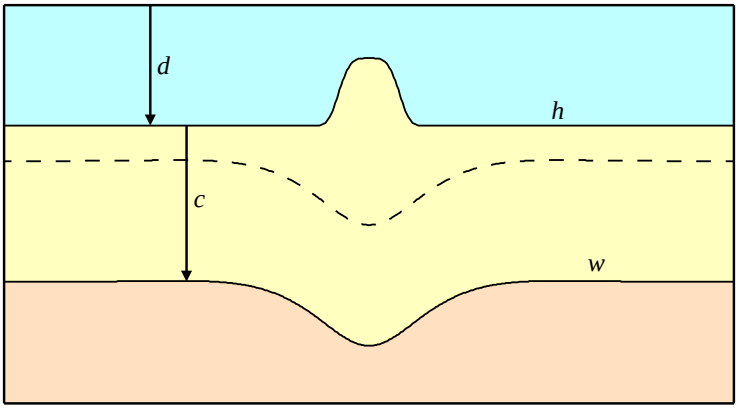

Figure C2. Cartoon cross-section through a seamount with flexural isostatic compensation as modeled by equation C11. Sea floor topography, *h*, loads the ocean lithosphere with a vertical normal stress $(\rho_h - \rho_w)gh$, causing it to bend into a shape, *w*; flexure of interfaces between layers of different densities in the crust provides the isostatic compensation of *h*.

The simple model in equation C11 places all the compensation at the Moho, the base of the crust, at a depth *c* below the *h* = 0 plane. Some authors included additional flexed layers (dashed line), resulting in small additional terms in C11.

$f(k)$ is often characterized by a parameter *H* called the "effective elastic thickness" of the lithosphere. From a theory for the flexure of a thin elastic membrane when $H << \lambda_f$ and $w << H$, one obtains

$$D = \frac{EH^3}{12(1-\nu^2)}, \qquad \text{(C12)}$$

in which *E* is Young's modulus and ν is Poisson's ratio. The literature is not consistent in the values used in (C12) and (C10) to relate *H* and Φ; one finds values of 0.8–1.0x10^{11} Pa for *E*, 0.22–0.25 for ν, 3330–3400 kg/m^3 for ρ_m, and 2600–2800 for ρ_h; we use *E* = 1.0x10^{11} Pa, ν = 0.25, ρ_m = 3330 kg/m^3, and ρ_h and ρ_w as above.

H varies in a complicated way in the oceans. Early studies of *H* at seamounts along the Hawaiian-Emperor chain concluded that *H* does not change systematically with seamount age (Watts and Cochran, 1974) but that *H* increases with the square root of the age difference between the seafloor age and the seamount age, the age of the seafloor when the topographic load formed (Watts, 1978). Watts et al. (1980) suggested that *H* is approximately one third of the seismic thickness of the lithosphere and is given approximately by the depth to the 450˚C isotherm if the lithosphere cools as in the model of Parsons and Sclater (1977). If some process limits the ultimate thickness of the lithosphere (Parsons and Sclater, 1977) then *H* would range between 0 and 40 km (Smith and Sandwell, 1994). Later studies (McNutt and Menard, 1982; McNutt, 1984; Calmant and Cazenave, 1987; Smith et al, 1989) found *H* values which did not follow Watts's rule; all were less than the rule would predict. Wessel (1992) reviewed these and proposed that thermal cooling stresses complicate the situation. However, the

flexural model, with H probably in the range of 0–40 km, is successful enough that it can be used to illustrate the basic relationship between g and h.

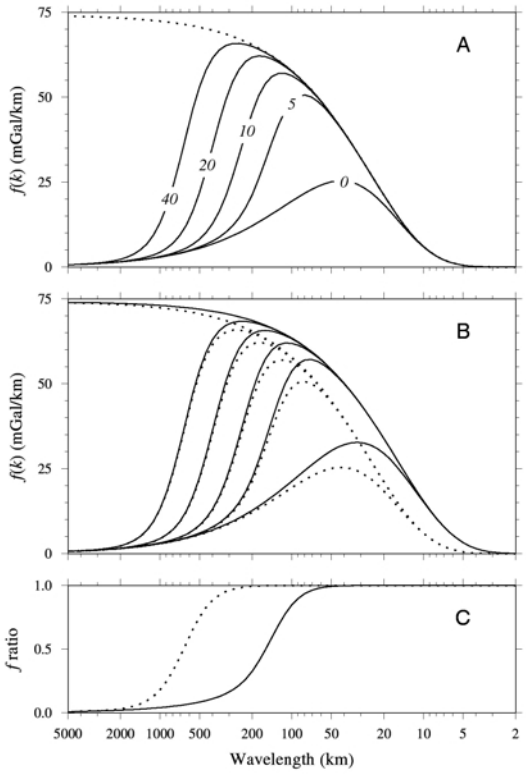

Fig. C3 Topography-to-gravity transfer function $f(k)$ from Eqn. C11. Top: for water depth d = 4 km. Numbers indicate effective elastic lithosphere thickness H. Dotted line indicates uncompensated situation (Eqn. C2). Middle: Comparison of d = 4 km (dotted lines) and d = 2.5 km (solid lines). Bottom: Ratios $f_5(k)/f_\infty(k)$ (solid) and $f_{40}(k)/f_\infty(k)$ (dotted) illustrate partitioning of wavebands; uncompensated structure band lies to the right of the solid curve.

Figure C3 (A) shows $f(k)$ values obtained from (C11) using the above densities, d = 4 km, and various H values. The dotted line is the case of no isostatic compensation (C2), which can also be viewed as infinite H. Figure C3 (B) shows the same curves obtained again with d = 4 km (dotted), and also d = 2.5 km (solid). These two panels of Figure C3 show that the gravity anomaly at sea level looks like a band-pass-filtered version of the sub-surface structure, with the filter parameters being d, c, and H in the flexure model. Figure C3 (C) shows how one might define wavelength bands and transitions between them based on these curves. The solid line is the ratio of $f_5(k)/f_\infty(k)$, and the dotted line is the ratio $f_{40}(k)/f_\infty(k)$, where the subscript on f indicates the H value used in that f. We have chosen H = 5 rather than H = 0 because in practice one always finds that the lithosphere has greater than zero strength. Watts et al. (1980) used H = 5 km for features formed on a ridge axis, (i.e. at zero age), and Cochran (1979) found H values of 2–6 km at the East Pacific Rise and 7–13 km at the Mid-Atlantic Ridge. The area between the two curves in Figure C3 (C) shows the range of wavelengths over which the gravity/topography ratio is sensitive to H; this has been called the "diagnostic waveband of flexural

response" by Watts and Ribe (1984). Since nearby topography features may have formed at different ages, each feature can have its own $f(k)$ (Watts et al., 1980). According to the flexural isostasy model, wavelengths of topography larger than the diagnostic band are supported by Airy floatation; various other support mechanisms can be described, each with its own $f(k)$; see Sandwell (1982). Thus the correlation between sea surface gravity and seafloor topography is easily understood only at wavelengths less than those in the band diagnostic of flexure, and this limits the band in which altimeter-derived gravity can be used to predict sub-surface structure to wavelengths shorter than those in the flexure band.

High-pass filters for the uncompensated band

Because the gravity field has a red spectrum, long-wavelength signals in it may dominate a gravity map, and for tectonic purposes it is useful to use a filter to enhance the shorter wavelengths. Smith and Sandwell (1994) used the function $f_5(k)/f_\infty(k)$ (actually a Gaussian approximation of it that was faster to compute) as a high-pass filter to isolate the uncompensated portion of the gravity field, where it is not necessary to know *H* in order to interpret the anomalies. They also used the converse low-pass filter on interpolated bathymetry in order to form a regional depth map. The half-amplitude transition of these filters is at a wavelength of 160 km. They "downward continued" (multiplied by $\exp[+kd]$) the high-pass-filtered gravity field to various levels *d*, and then interpolated the downward-continued *g* solutions onto the low-pass-filtered regional depth, in effect "draping" the high-pass-filtered *g* over the long-wavelength variations in *d*. Downward continuation is unstable at short-wavelengths (large *k*) and so Smith and Sandwell (1994) used the SNR information from repeat track altimetry to design a stabilizing filter that minimizes the mean square error of downward continuation. In Figure C4 we have applied the same process to the Sandwell & Smith (1997) gravity field, to allow variations in the amplitude of *g* in the uncompensated band to be compared between areas which lie at different depths.

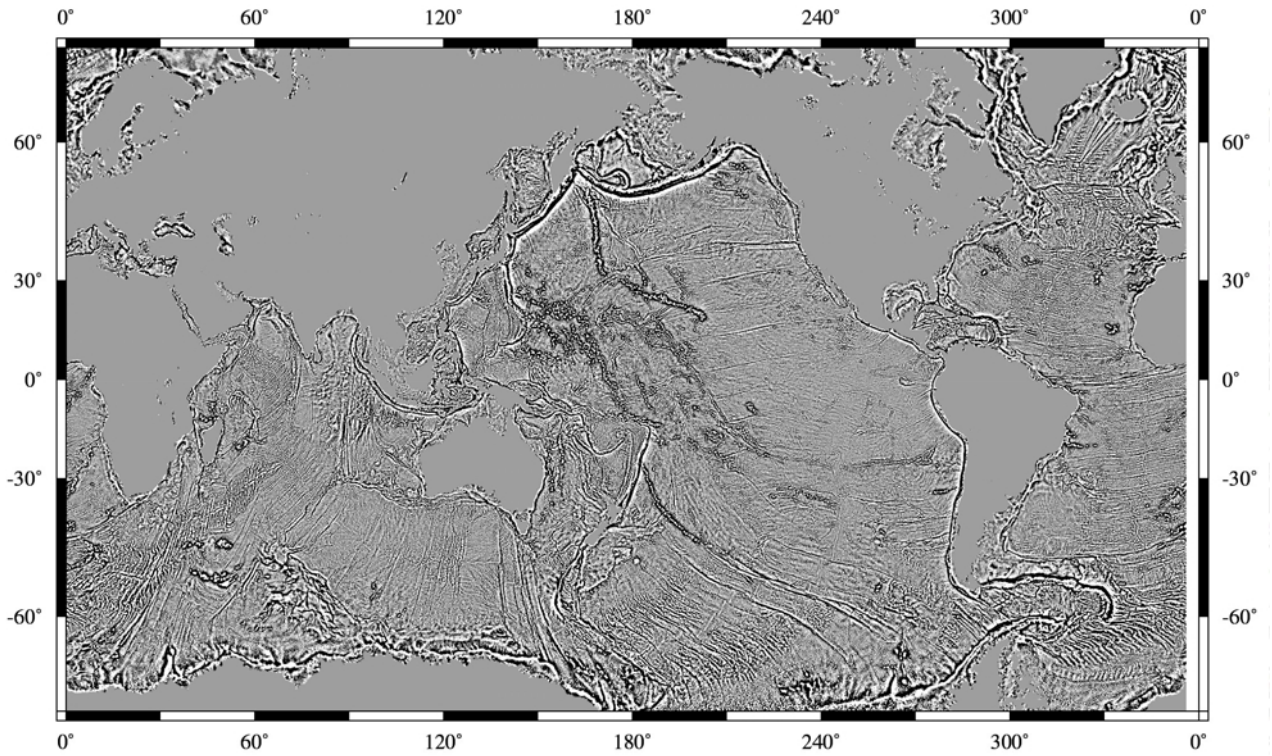

Figure C4. Band-pass-filtered and downward-continued gravity anomalies allow comparison of amplitudes in the uncompensated band independent of the attenuating effect of regional depth.

Correlation between gravity and sea floor topography

The topography generated by tectonic processes at mid-ocean ridges gradually becomes buried under sediment. If the sediment cover is sufficiently thick, the seafloor may be flat. Gravity anomalies will still be seen, although with diminished amplitude; these come from sub-seafloor structures, particularly basement topography. Since the density contrast between basement rocks and sediments is generally much less than the density contrast between seafloor materials and seawater, g is usually correlated with sea floor topography wherever the sea floor has thin sediment. A complicated and non-linear correlation is expected when the basement topography is partially buried, with structural highs exposed and troughs filled with sediment. Smith and Sandwell (1994; 1997) computed the correlation between high-pass-filtered ship surveys of depth and high-pass-filtered and downward-continued gravity in order to determine the correlation and proportion between these two quantities, which they exploited in order to estimate detailed bathymetry from altimeter-derived gravity. High correlations (Fig. C5) occur in most areas except over very smooth seafloor, such as over abyssal plains. Liu et al. (1982) give an interesting example of the gravity anomaly due to a tectonic structure buried under flat seafloor.

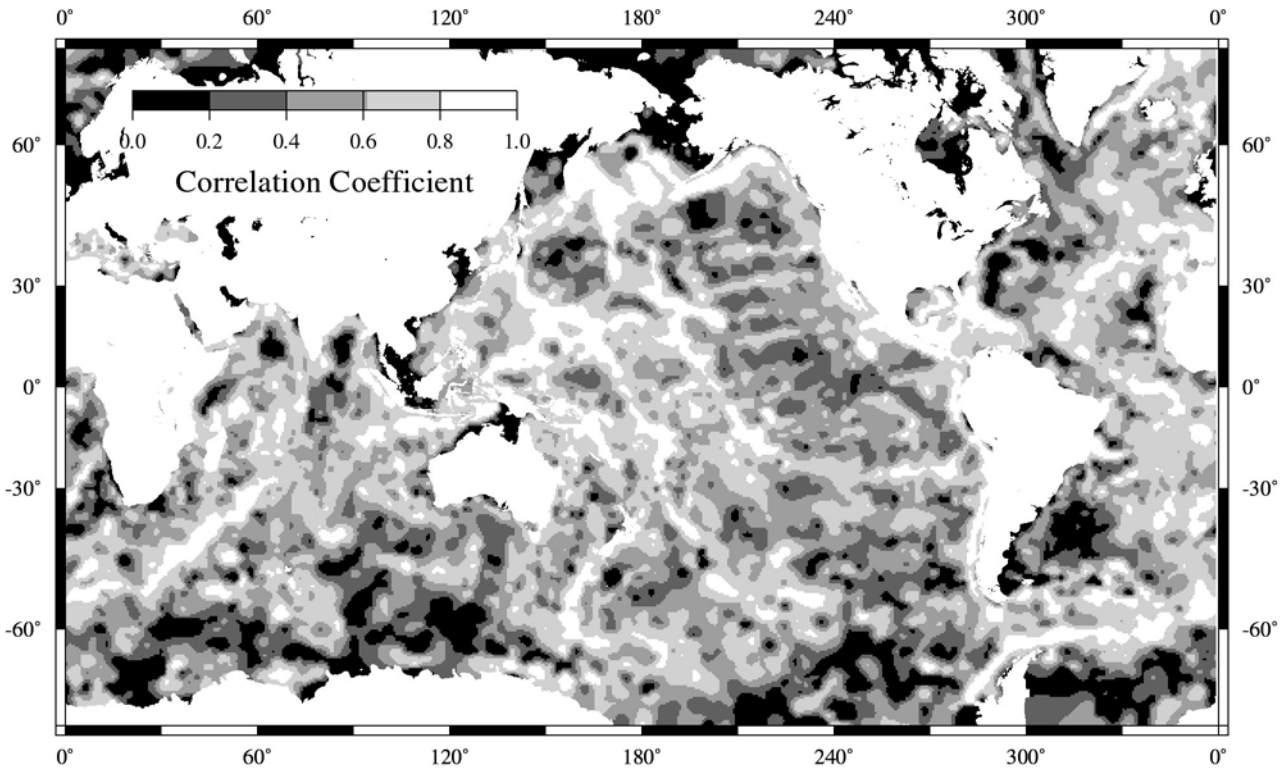

Figure C5. Correlation between seafloor depth and sea surface gravity after bandpass filters and downward continuation have been applied. Correlations are high where the ocean floor is thinly sedimented and high-amplitude topography generated by seafloor spreading at a mid-ocean ridge. Correlations are low where amplitudes are low and over sedimentary basins, where the gravity anomalies reflect sub-seafloor structures in the basins and not seafloor topography.

Prediction of bathymetry from gravity

Because altimetry furnishes complete gravity data coverage in map view, while ship soundings are sparse in many areas, one would like to exploit the gravity-topography correlation to use gravity to predict bathymetry. If one seeks a linear operator to do this, it would have a form the inverse of equation (C3), and the transfer function would look like the reciprocal of those in Figure C3. Such a function would become arbitrarily large at both very long wavelengths and very short wavelengths, due to isostasy and upward continuation, respectively. Therefore one may hope to use altimetry to recover bathymetry only in a limited band of wavelengths, and the transfer function must have the form of a band-pass-filtered version of the inverse of equation (C11) or a similar equation.

The best linear operator projecting one data type into another can be found by Wiener filter theory, if by "best" one means minimizing the mean square error of the estimate. Wiener filtering requires knowledge of the signal-to-noise ratio in the input data as a function of wavelength or frequency. Smith and Sandwell [1994] designed filters for projecting gravity in the uncompensated band (Figure C4) into estimated seafloor topography using the Wiener optimization scheme. They then used existing sounding data to test for correlations (Figure C5) and calibrate scale factors which account for the presence of sediment cover on the basement topography. After calibration the result is an estimate of the seafloor

topography in the band of wavelengths where topography is uncompensated and signal-to-noise ratios in altimetry are high enough to be passed by the Wiener filter. This estimated topography was then combined with a low-pass-filtered regional depth map they obtained from interpolated soundings to yield the total bathymetry shown in Figure 1.2.

To test the method, the results can be compared against actual soundings. Figure C6 shows three versions of depth along the track of the R/V Atalante from a 1997 GPS-navigated cruise through an area near the Foundation Seamounts, which are in the Pacific Ocean west of the Easter microplate. The top profile (**A**) shows the topography according to the ETOPO5 model [*National Geophysical Data Center*, 1998], the middle profile (**B**) shows the actual sounding data from the center beam of the Simrad 12D multibeam system on board Atalante, and the bottom profile (**C**) shows the topography predicted from altimetry by Smith and Sandwell [1997] using the Wiener-optimized method. While altimetry fails to capture the full amplitude of some seamounts and troughs, it follows the actual topography much more closely than the ETOPO5 model, which was produced by gridding digitized contour maps based on old data.

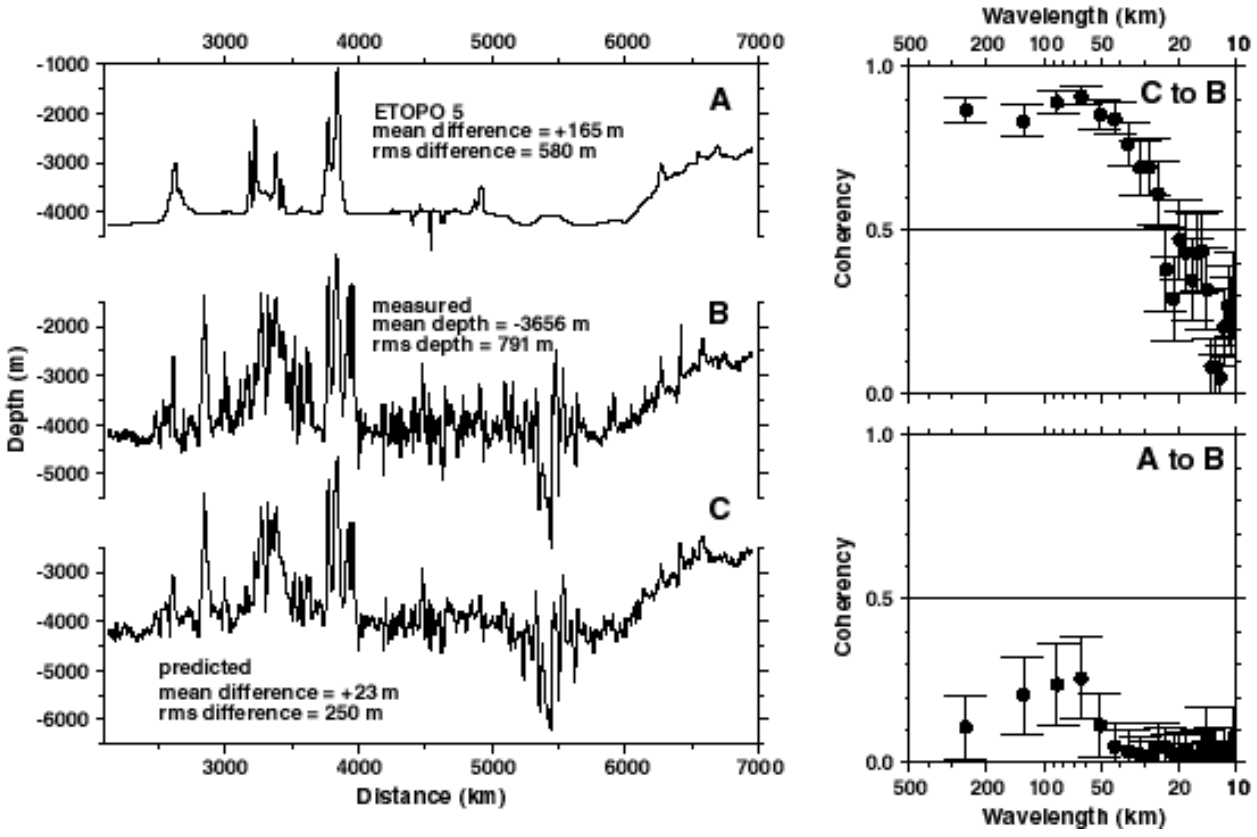

Figure C6. (left) Depth along the cruise track of the Atalante. **A**-according to ETOPO5. **B**-as measured by the ship's multibeam system and **C**-as predicted from altimetry. (right) Cross-spectral coherency between topographic profiles. A value of 0.5 means signal and noise power are equal in magnitude, larger values are coherent and smaller values are incoherent. A-between ground truth (Profile **B**) and altimeter-estimates (Profile **C**). **B**-between ground truth and ETOPO5 model (Profile **A**).

The resolution of altimeter-predicted depth as a function of wavelength can be assessed with a cross-spectral comparison between profiles **C** and **B** of Figure C6. The (squared) coherency between the two is shown in the right panel of Figure C6. Assuming that there is no noise in the sounding data and all the differences between the altimeter-predicted depths and the soundings are due to noise in the altimeter data, then the wavelength at which the coherency equals 1/2 is that at which the signal-to-noise ratio in the altimeter predictions equals one (Bendat and Piersol, 1986, equation 6.39); this is about 20 km. At longer wavelengths the coherency is higher and the altimeter-derived estimates agree well with the ground truth; at shorter wavelengths the coherence is poor and the altimetry is not resolving the actual bathymetry. Figure C6 (**A** to **B**) shows the coherency between the actual soundings and the ETOPO5 model for comparison. It is clear that ETOPO5 does not resolve the actual depth at any wavelength.

The limiting resolution of 24 km shown here is expected, for two reasons. First, the mean depth along these profiles is about 3.5 km, and 2π times this value is about 22 km, so upward continuation theory suggests that the gravity signal of the topography will be attenuated at wavelengths which are short compared to 22 km. Second, the altimeter-predicted values shown here were obtained with the Wiener-optimized filters of Smith and Sandwell [1994], and these filters attenuate signals shorter than 20 km, because this is where analysis of the repeatability of altimeter measurements shows that their signal-to-noise ratios are around 1 to 1. (See Section 3 and Figure 3.2). Therefore altimetry will resolve shorter wavelengths in seafloor structure only if the signal-to-noise ratio in the data can be improved, and strongly enough to keep up with the upward continuation. Or, viewed another way, a given improvement in altimeter signal-to-noise will yield the most dramatic improvement in resolution where the mean ocean depth is shallow, such as on the continental margins.

Appendix D. Environmental corrections converted to sea surface slope

(Appendix modified from Mara Yale's Ph.D., Thesis,
Yale, M. M., *Modeling Upper Mantle Rheology with Numerical Experiments and Mapping Marine Gravity with Satellite Altimetry,* Ph. D. Thesis, Univ. of California, pp. 118, San Diego, 1997.)

Measurements of the height of the ocean surface above the reference ellipsoid can be corrupted by a number of environmental factors including:

- ocean tide (corrected with tide measurement or tide model);
- solid earth tide (corrected with tide model);
- dry tropospheric delay (corrected with atmospheric pressure/temperature measurement or model);
- wet tropospheric delay (corrected with microwave radiometer measurement or model);
- inverted barometer effect (corrected with surface pressure measurement or model);
- ionospheric delay (corrected with dual frequency altimeter measurement or model);
- and electromagnetic bias (corrected with the shape of radar return and calibration).

The environmental corrections supplied with TOPEX data were used to determine which corrections are important when recovering marine gravity anomaly from sea surface slope measurements. As shown in Appendix B, one microradian (μrad) of slope error corresponds to one mGal of marine gravity error so we should be concerned when the slope of the correction exceeds about 0.5 μrad. The important issue for spacecraft design is that if the slope of the correction is less than 0.5 μrad, then it is unnecessary to provide the measurement capability onboard the spacecraft. TOPEX/Poseidon spacacraft was able to measure the wet tropospheric delay and ionospheric delay using a microwave radiometer and a second radar altimeter operating at C-band, respectively. We show that these instruments are unnecessary for an altimeter mission that is focussed on gravity field recovery because the sea-state effects are larger than the corrections.

D.1 *Analysis of TOPEX/Poseidon Environmental Corrections*

To assess the slope of the environmental corrections for the TOPEX altimeter, we output (cycle 17 only) the measurement time, latitude, longitude, and the slopes of the supplied environmental corrections including: ocean tide, solid earth tide, dry troposphere, wet troposphere, inverted barometer, ionosphere, and electromagnetic bias (embias). The slope of each correction is the difference between corrections given each second, divided by 5.8 km. (Topex travels at ~5.8 km/s over the ground.) The slope correction amplitudes were then averaged in 1-degree by 1-degree cells, and gridded to create maps showing their geographic distribution. (Note that the maps below have gridding problems in the areas of Hudson Bay, Labrador Sea, and Sea of Okhotsk due to sea-ice problems and data dropouts.) We also plotted histograms of the absolute value of the slope of each correction for the entire 10-day cycle.

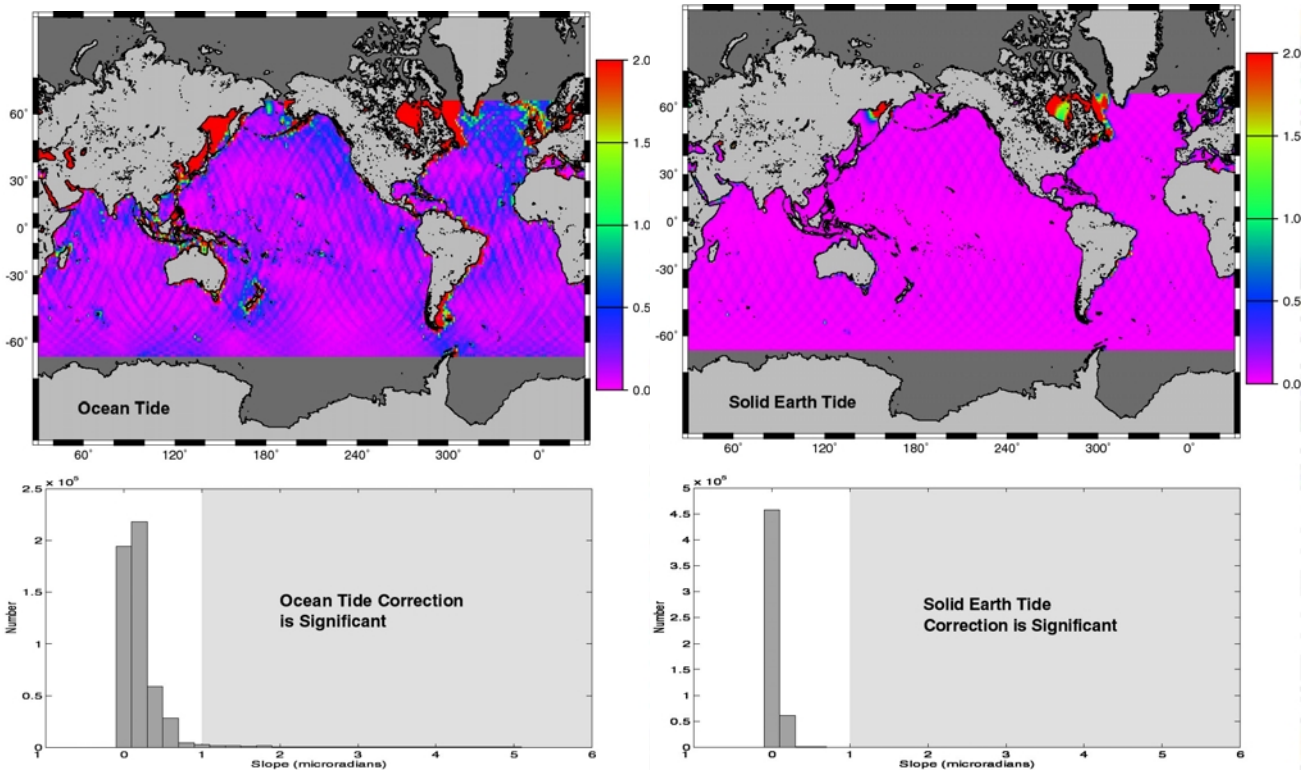

Figure D.1 (left) Map and histogram of ocean tide correction slopes
Figure D.2 (right) Map and histogram of solid Earth tide correction slopes

We conclude that the only correction needed to achieve the 1 μrad accuracy is the ocean tide. Slopes of the ocean tide exceed 2 μrad on most of the continental shelves (Figure D.1) and in several areas the tidal slopes exceeds 4 μrad [*Sandwell and Smith*, 1997]. This correction can be computed from global tide models [e.g., *Bettadpur and Eanes*, 1994] although the models are sometimes inaccurate in the shallow areas of the oceans and inland seas. The maps and histograms for the solid earth tide (Figure D.2), dry troposphere (Figure D.3), wet troposphere (Figure D.4), and inverted barometer (Figure D.5) reveal that the amplitude of correction slopes for these environmental corrections is less than 0.5 μrad almost everywhere.

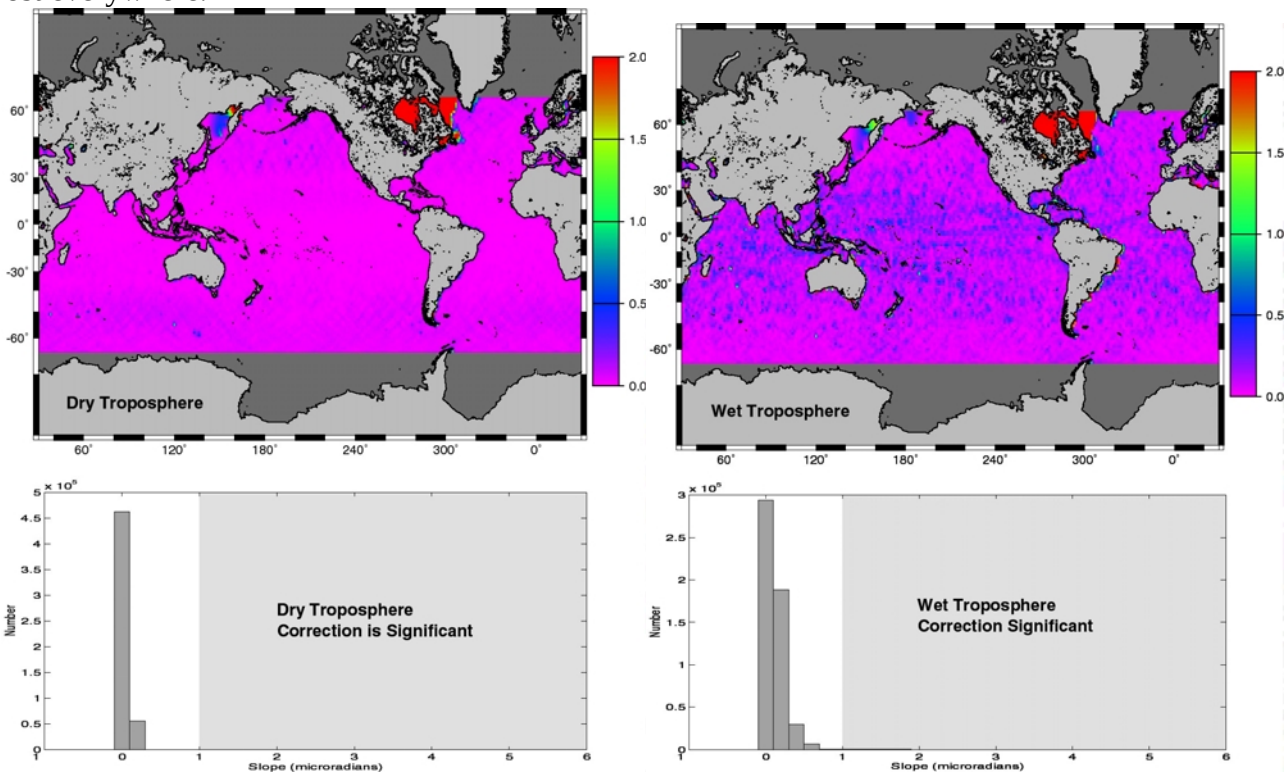

Figure D.3 (left) Map and histogram of dry troposphere correction slopes
Figure D.4 (right) Map and histogram of wet troposphere correction slopes

TOPEX has a dual frequency altimeter that is supposed to be capable of measuring the delay due to the ionosphere. However, the map of the ionosphere slope correction (Figure D.6) reveals a pattern that looks like a map of sea state. The ionosphere slope correction is high at high latitudes, and lower in the calmer equatorial waters. In contrast, the map of ionospheric slope correction supplied by the Bent model of the ionosphere (Figure D.8) shows several bands of higher slope in the equatorial region where the electrojet causes a spatial variation in the number of electrons present in the ionosphere. In order to validate the ionospheric slope correction that is measured with the dual frequency altimeter, we filtered the TOPEX slope correction with a 5 point boxcar filter. (Note *Imel* [1994] recommends a 24-point filter

to reduce the sea-state effects.) The map of the filtered slope correction is flat, with most slope correction at or below 0.5 μrad (Figure D.7).

To understand this effect of sea state on the ionospheric correction, consider how the ionospheric correction is measured. The ionosphere is dispersive so the time delay of a radar pulse (group velocity) depends on the free-electron density integrated along the path (i.e., the total electron content, TEC) and is inversely proportional to the square of the frequency of the EM wave. Thus, the time delay difference between C and Ku bands can be used the correct the total time delay in the Ku-band. However, this assumes there are no other frequency-dependent errors. When the sea state is rough, the C and Ku bands are scattered differently which introduces a wave height-dependent noise in the time difference measurement (*Imel*, 1994). The conclusion is that while the ionospheric correction is accurate and important for sea surface height measurements over wavelengths greater than about 100 km, it adds noise to the shorter wavelength measurement of sea surface slope.

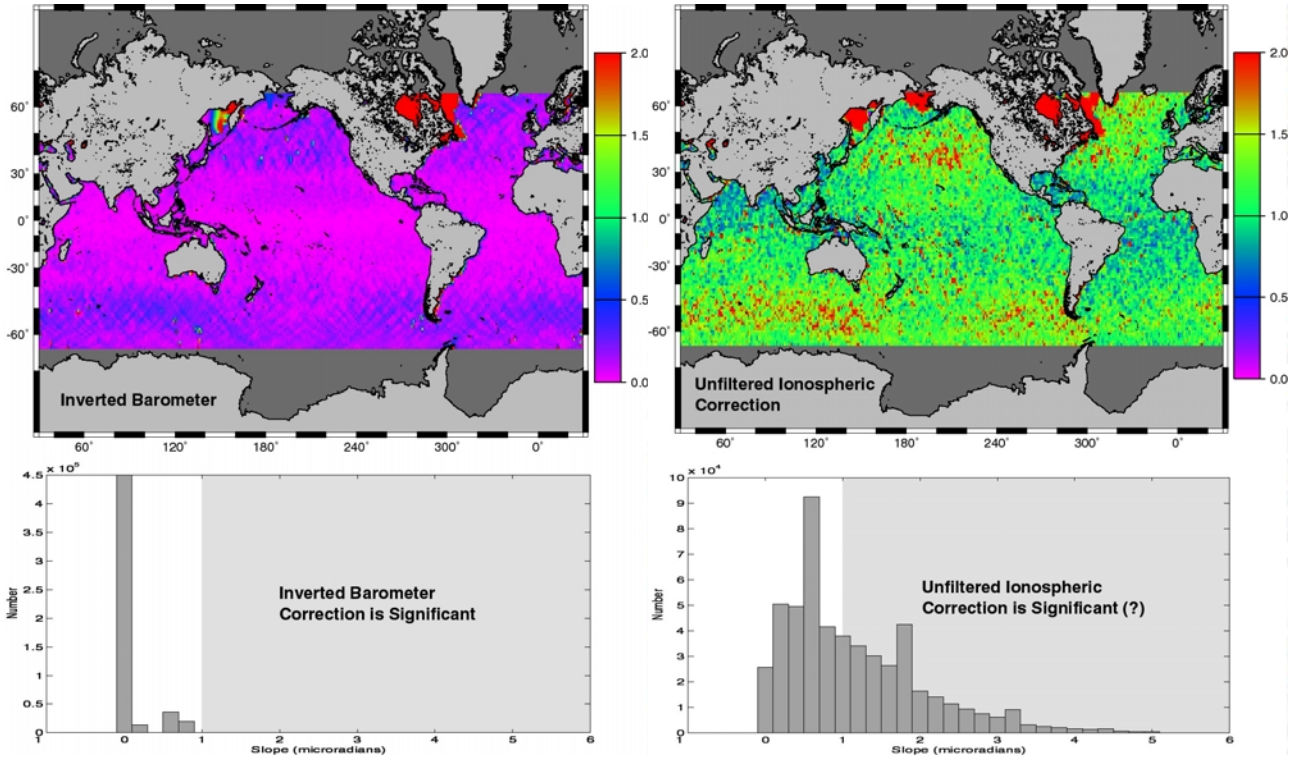

Figure D.5 (left) Map and histogram of inverted barometer correction slopes
Figure D.6 (right) Map and histogram of ionosphere correction slopes (TOPEX 2 freq.)

Finally, the embias correction is measured by modeling the returned waveform to determine the Significant Wave Height (SWH) (Figure D.9). The EM bias is a small fraction of the SWH (e.g. 4%). As for the ionosphere, we filtered the embias correction slopes with a 5 point boxcar, and the map of the filtered correction slopes (Figure D.10) is flat with most correction slopes below 0.5 μrad. The EM bias slope correction is important when wave heights are large but in this case, the errors in the along-track slope measurement will also be large so the correction is useless.

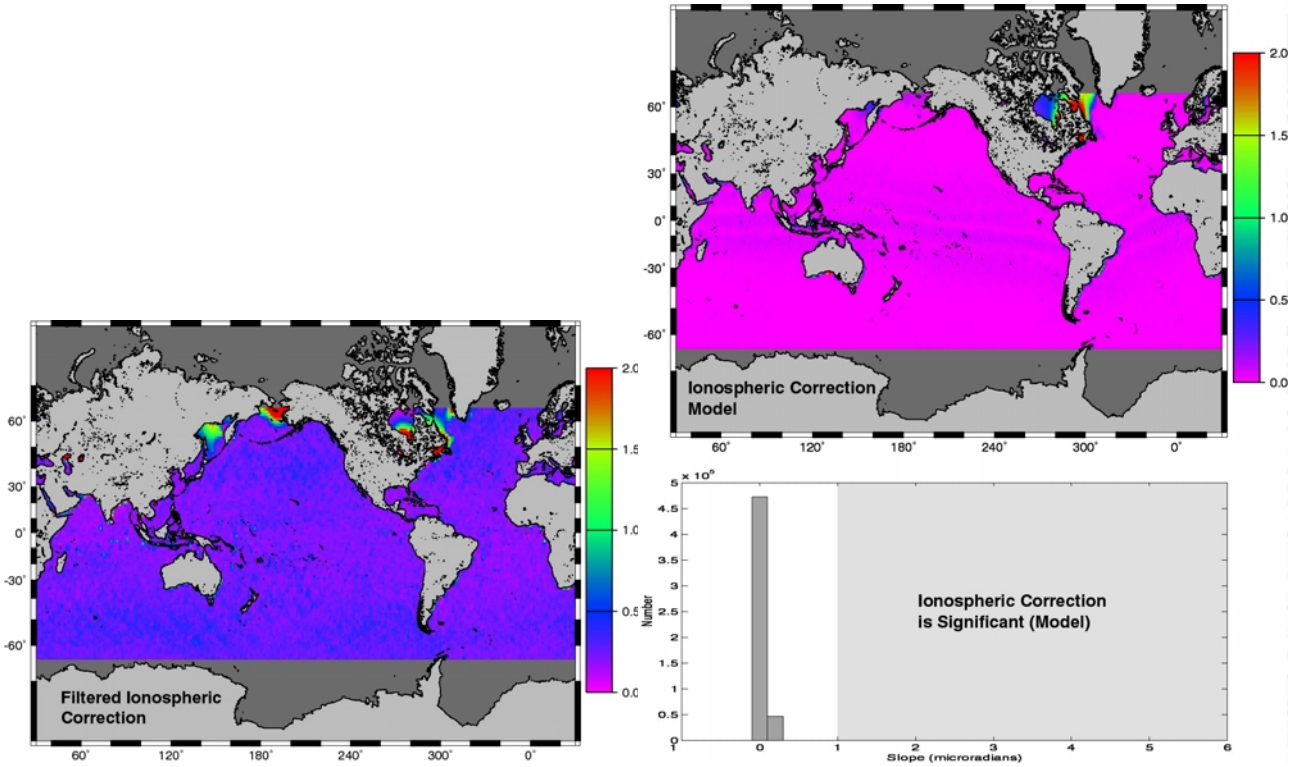

Figure D.7 (left) Map ionosphere correction slopes (TOPEX 2 freq.), filtered
Figure D.8 (right) Map and histogram of ionosphere correction slopes (Bent model)

In summary, both the ionosphere correction slopes and embias correction are large in regions of high sea state. This indicates that the high sea state decreases the measurement accuracy, and thus the corrections are poorly determined. The conclusion is that the ocean surface waves introduce noise in the along-track slope measurement that cannot be eliminated.

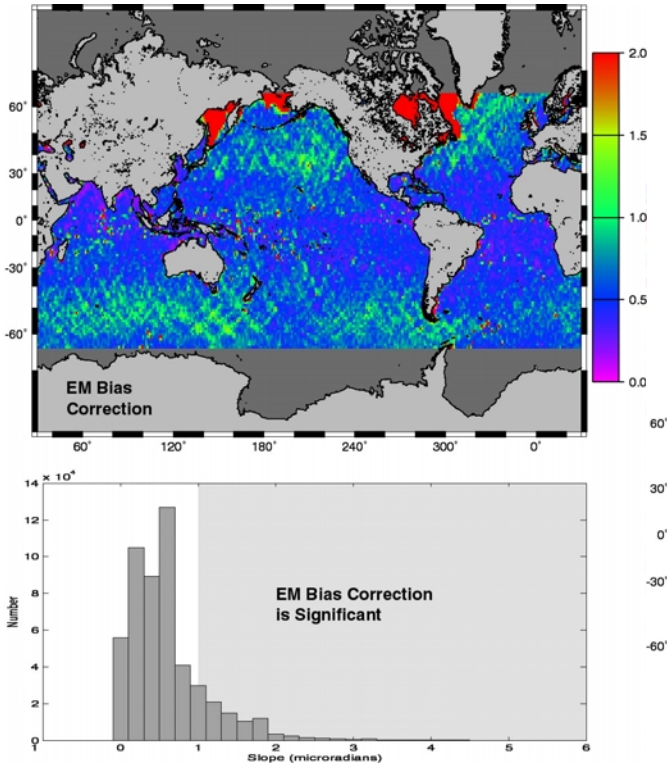

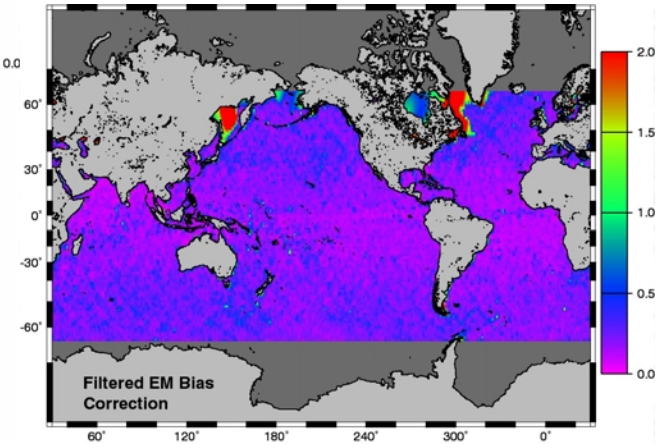

Figure D.9 (left) Map and histogram of embias correction slopes

Figure D.10 (right) Map of embias correction slopes, filtered

References

Abbott D. (1986). A statistical correlation between ridge crest offsets and spreading rate. *Geophys. Res. Lett.* **13**:157--60

Airy, G. B. (1855). On the computations of the effect of the attraction of the mountain masses as disturbing the apparent astronomical latitude of stations in geodetic surveys, *Trans. R. Soc. London B*, v. **145**.

Banks, R. J., Parker, R. L., and Huestis, S. P. (1977). Isostatic compensation on a continental scale: Local versus regional mechanisms. *Geophys. J. R. astr. Soc*. **51**, 431-452.

Barrell J. (1914-15). *The Strength of the Earth's Crust.* A privately printed collection of reprints of articles originally appearing in the J. Geol. 22:28--48, 145--65, 209--36, 289--314, 441--68, 537--55, 655--83, 729--41 (1914); and 25:27--44, 424--443, 499--515 (1915). Available from the library of the National Oceanic and Atmospheric Administration, Silver Spring MD USA.

Baudry, N., and Calmant, S. (1991). 3-D Modeling of seamount topography from satellite altimetry. *Geophys. Res. Lett.* **18**, 1143-1146.

Bouguer, P. (1749). *La figure de la terre*. Paris.

Bendat JS, Piersol, A. G. (1986. *Random Data---Analysis and Measurement Procedures*. New York: Wiley & Sons. 566 pp. 2nd ed.

Bettadpur, S. V., R. J. Eanes, R. J. (1994). Geographical representation of radial orbit perturbations due to ocean tides: Implications for satellite altimetry. *J. Geophys. Res*. **99**, 24,883-24,898.

Calmant, S. (1994). Seamount topography of least-squares inversion of altimetric geoid heights and shipborne profiles of bathymetry and/or gravity anomalies. *Geophys. J. Int*. **119**, 428-452.

Calmant S, Cazenave A. (1987). Anomalous elastic thickness of the oceanic lithosphere in the south-central Pacific. *Nature* **328**:236--8

Canadian Hydrographic Service (1981). *General bathymetric Chart of the Oceans (GEBCO)*. Hydrographic Chart Distribution Office, Ottawa, Canada.

Cazenave, A., Royer J-Y, (2001). Applications to Marine Geophysics, *in Satellite Altimetry and Earth Sciences*, edited by L.-L. Fu and A. Cazenave, Intl. Geophys. Series., vol **69**, Academic Press, New York, 407-435.

Cazenave, A., Schaeffer, P., Berge, M., and Brossier, C. (1996). High-resolution mean sea surface computed with altimeter data of ERS-1 (Geodetic Mission) and TOPEX-POSEIDON. *Geophys. J. Int*. **125**, 696-704.

Chelton, D. B., Schlax, M. G., Witter, D. L., and Richman, J. G. (1990). Geosat altimeter observations of the surface circulation of the Southern Ocean. *J. Geophys. Res*. **95**, 17,877-17,903.

Chen Y-J, Morgan WJ. (1990a). Rift valley / no rift valley transition at mid-ocean ridges. *J. Geophys. Res.* **95**:17571--83

Chen Y-J, Morgan WJ. (1990b). A nonlinear rheology model for mid-ocean ridge axis topography. *J. Geophys. Res.* **95**:17583--604

Christensen, et al. (1994). Calibration of TOPEX/POSEIDON at Platform Harvest. *J. Geophys. Res*. **99**, 24,465-24,486.

Cochran JR. (1979). An analysis of isostasy in the world's oceans, 2, mid-ocean ridge crests. *J. Geophys. Res*. **84**:4713-4729

Devey, C., et al. (1997). The Foundation Seamount Chain: A first survey and sampling. *Mar. Geol*. **137**, 191-200.

Dixon, T. H., Naraghi, M., McNutt, M. K., and Smith, S. M. (1983). Bathymetric prediction from Seasat altimeter data. *J. Geophys. Res*. **88**, 1563-1571.

Dorman LM, Lewis BTR. (1970). Experimental isostasy, 1, Theory of the determination of the earth's isostatic response to a concentrated load. *J. Geophys. Res*. **75**:3357—3365

Dressler, B.O., Sharpton, V. *Large Meteorite Impacts and Planetary Evolution; II*, Special Paper 339, Geological Society of America, Boulder, CO.

Egbert, G. D. and R. D. Ray (2000). Significant dissipation of tidal energy in the deep ocean inferred from satellite altimeter data. *Nature* **405**, 775–778.

Feldman, G., D. Clark, and D. Halpern, (1984): Satellite color observations of the phytoplankton distribution in the eastern equatorial Pacific during the 1982-1983 El Nino. Science, **226**, 1069-1071.

Gahagan LM, Scotese CR, Royer JY, Sandwell DT, Winn JK, Tomlins RL, et al. (1988). Tectonic fabric map of the ocean basins from satellite altimetry data. *Tectonophys*. **155**:1—26.

Geli, L; Aslanian, D; Olivet, JL; Vlastelic, I; Dosso, L; Guillou, H; Bougault, H. (1998) Location of Louisville hotspot and origin of Hollister ridge: Geophysical constraints. Earth, Planet. Sci. Lett.,*164(N1-2):*31-40.

Gille, S. T. (1994). Mean sea surface height of the Antarctic circumpolar current from Geosat data: Method and application. *J. Geophys. Res*. **99**, 18,255-18,273.

Gille, S. T. and K. A. Kelly (1996), Scales of spatial and temporal variability in the Southern Ocean, *J. Geophys. Res*., **101**, 8759-8773.

Gille, S. T., Yale, M. M., and Sandwell, D. T. (2000). Global correlation of mesoscale ocean variability with seafloor roughness from satellite altimetry. *Geophys. Res. Lett.* **27**, 1251–1254.

Goff JA, Jordan TH. 1988. Stochastic modeling of seafloor morphology: inversion of Sea Beam data for second-order statistics. *J. Geophys. Res*. **93**:13589--608

Gordon, A. L., and Baker, T. N. (1986*). "Southern Ocean Atlas." Published for the International Decade of Ocean Exploration, National Science Foundation.*

Gunn R. (1943). A quantitative study of isobaric equilibrium and gravity anomalies in the Hawaiian Islands. *Franklin Inst. J.* **236**:373--90

Haxby, W. F., Karner, G. D., LaBrecque, J. L., and Weissel, J. K. (1983). Digital images of combined oceanic and continental data sets and their use in tectonic studies. *EOS Trans. Amer. Geophys. Un*. **64**, 995-1004.

Hayne, G. S., Hancock, D. W., Purdy, C. L., and Callahan, P. S. (1994). The corrections for significant wave height and altitude effects in the TOPEX radar altimeter. *J. Geophys. Res*. **99**, 24,941-24,955.

Heezen et al., 1959.

Heiskanen, W. A., and H. Moritz, H. (1967). *Physical Geodesy*. W. H. Freeman and Co., San Francisco.

Heiskanen WA, Vening Meinesz FA. (1958). *The Earth and its Gravity Field*. New York: McGraw-Hill. 470 pp.

Holloway, G., (1992). Representing topographic stress for large scale ocean models, *J. Phys. Oceanogr*., **22**, 1033-1046.

Holcome and Moore, (2000).

Hwang, C., Kao, E.-C., and Parsons, B. (1998). Global derivation of marine gravity anomalies from Seasat, Geosat, ERS-1 and TOPEX/POSEIDON altimeter data. *Geophys. J. Int*. **134**, 449-459.

Hwang, C., and Parsons, B. (1996). An optimal procedure for deriving marine gravity from multi-satellite altimetry. *J. Geophys. Int*. **125**, 705-719.

Imel, D.A. (1994). Evaluation of the TOPEX/POSEIDON dual-frequency ionospheric correction. *J. Geophys. Res.* **99**, 24,895-24,906.

Jayne, S. R., and L. C. St. Laurent (2001). Parameterizing tidal dissipation over rough topography. *Geophys. Res. Lett.* **28**, 811–814.

Jung, W. Y., and Vogt, P. R. (1992). Predicting bathymetry from Geosat-ERM and shipborne profiles in the South Atlantic ocean. *Tectonophysics* **210**, 235-253.

Kelly, K. A., (1991). The meandering Gulf Stream as seen by the Geosat altimeter: Surface transport, position, and velocity variance from 73 to 46W, *J. Geophys. Res.*, **96**, 16,721-16,738.

Laxon, S., and McAdoo, D. (1994). Arctic ocean gravity field derived from ERS-1 satellite altimetry. *Science* **265**, 621-624.

LaCasce, J. H. (2000). Floats and *f/H*. *J. Mar. Res*., **58**, 61-95.

Ledwell, J. L., E. T. Montgomery, K. L. Polzin, L. C. St laurent, R. W. Schmitt and J. M. Toole, (2000). Evidence for enhanced mixing over rough topohraphy in the abyssal ocean, *Nature, 403, (6766),* 179-182.

Lemoine, F. G., et al. (1998). The development of the joint NASA CSFC and the national Imagery and Mapping Agency (NIMA) geopotential model EGM96. Goddard Space Flight Center, NASA, NASA/TP-1998-206861.

Liu, C.-S., Sandwell, D. T., and J. R. Curray, J. R. (1982). The negative gravity field over the 85˚ Ridge. *J. Geophys. Res.*, **87**, 7673-7686.

Livermore R, McAdoo D, Marks K. (1994). Scotia Sea tectonics from high-resolution satellite gravity. *Earth Planet. Sci. Lett.* **123**:255-268

Maia, M., et al. (2000). The Pacific-Antarctic Ridge-Foundation hotspot interaction: a case study of a ridge approaching a hotspot, *Marine Geology, v. 167,* p. 61-84

Malinverno A. (1991). Inverse square-root dependence of mid-ocean ridge flank roughness on spreading rate. *Nature* **352**:58—60.

Mammerickx, J. (1992). The Foundation Seamounts: tectonic setting of a newly discovered seamount chain in the South Pacific. *Earth Planet. Sci. Lett*. **113**, 293-306.

Marks, K. M. (1996). Resolution of the Scripps/NOAA marine gravity field from satellite altimetry. *Geophys. Res. Lett*. **23**, 2069-2072.

Marks KM, Stock JM. (1994). Variations in ridge morphology and depth-age relationships on the Pacific-Antarctic Ridge. *J. Geophys. Res*. **99**:531--41

Marks KM, Stock JM. (1995). Asymmetric seafloor spreading and short ridge jumps in the Australian-Antarctic Discordance. *Marine Geophys. Res.* **17**:361--73

Maus, S., Green, C. M., and Fairhead, J. D. (1998). Improved ocean-geoid resolution from retracked ERS-1 satellite altimeter waveforms. *Geophys. J. Int*. **134**, 243-253.

McCartney, M. S., (1976). The interaction of zonal currents with topography with applications to the Southern Ocean, Deep Sea Res., **23**, 413-427.

Macdonald KC. (1986). The crest of the Mid-Atlantic Ridge: Models for crustal generation processes and tectonics, in *The Geology of North America, vol. M, The Western North Atlantic Region*, ed. by PR Vogt and BE Tucholke, Boulder, Colo.: Geol. Soc. Amer.

McKenzie, D. P. (1976). Some remarks on heat flow and gravity anomalies. *J. Geophys. Res.* **72**, 6261-6273.

McKenzie, D. P., and Bowin, C. (1976). The relationship between bathymetry and gravity in the Atlantic Ocean. *J. Geophys*. Res. **81**, 1903-1915.

McNutt, M. (1979). Compensation of oceanic topography: An application of the response function technique to the Surveyor area. *J. Geophys. Res*. **84**, 7589-7598.

McNutt M. (1984). Lithospheric flexure and thermal anomalies. *J. Geophys. Res*. **89**:11180--94

McNutt M, Menard HW. (1982). Constraints on yield strength in the oceanic lithosphere derived from observations of flexure. *Geophys. J. Roy. Astron. Soc*. **71**:363—83.

Mayes C.L; Lawver L.A and Sandwell D.T. (1990). Tectonic history and new isochron chart of the South Pacific, *J. Geophys., Res., v. 95*, p. 8543-8567.

Medea, (1995) Scientific Utility of Naval Environmental Data. MEDEA Office.

Menard, (1958)

Menard, (1964)

Menard HW. (1967). Seafloor spreading , topography, and the second layer. *Science* 157:923--4

Menard, H. W., and Smith, S. M. (1966). Hypsometry of Ocean Basin Provinces. *J. Geophys. Res*. **71**, 4305-4325.

Monahan , 2000, Monahan et al., 1999, Monahan and Wells, 1999,

Morrow, R., Church, J., Coleman, R., Chelton, D., and N. White, N. (1992). Eddy momentum flux and its contribution to the Southern Ocean momentum balance. *Nature* **357**, 482-484.

Mueller, R. D., Roest, W. R., Royer, J.-Y., Gahagan, L. M., and Sclater, J. G. (1997). Digital isochrons of the world's ocean floor. *J. Geophys. Res*. **102**, 3211-3214.

Müller, R. D., Smith, W. H. F. (1993). Deformation of the oceanic crust between the North American and South American plates, *J. Geophys. Res*. **98**: 8275–8291

Munk & Wunsch (1997). Abyssal recipes II: energetics of tidal and wind mixing, *Deep-sea Research Part I, **45***, p. 1977-2010.

Munk & Wunsch (1997). The Moon of course, *Oceanography, V. 10*, p. 132-134.

National Geophysical Data Center. (1988). ETOPO-5 bathymetry/topography data. *Data Announc. 88-MGG-02*. Boulder, Colo.: Nat'l Oceanic and Atmos. Admin., U.S. Dept. Commer.

Nettleton, L. L. (1939). Determination of Density for Reduction of Gravity Observations. *Geophysics* **4**, 176-183.

Noreus, J. P. (1995). Improved resolution of Geosat altimetry using dense sampling and polynomial adjusted averaging. *Int. J. Remote Sensing* **16**, 2843-2862.

Olgiati A, Balmino G, Sarrailh M, Green CM. (1995). Gravity anomalies from satellite altimetry: comparison between computation via geoid heights and via deflections of the vertical. *Bull. Geod.* **69**:252--60

Parker, R. L. (1973). The rapid calculation of potential anomalies. *Geophys. J. R. astr. Soc*. **31**, 447-455.

Parker, R. L. (1994). "Geophysical Inverse Theory." Princeton University Press, Princeton.

Parsons, B. (1982). Causes and consequences of the relation between area and age of the ocean floor. *J. Geophys. Res*. **87**, 289-302.

Parsons, B., and Sclater, J. G. (1977). An analysis of the variation of the ocean floor bathymetry and heat flow with age. *J. Geophys. Res*. **82**, 803-827.

Phipps Morgan et al., (1987).

Phipps Morgan J, Chen YJ. (1992). Dependence of ridge-axis morphology on magma supply and spreading rate. *Nature* **357**:706--8

Phipps Morgan J, Chen YJ. (1993). The genesis of oceanic crust: magma injection, hydrothermal circulation, and crustal flow. *J. Geophys. Res.* **98**:6283—98.

Phipps Morgan J, Parmentier EM. (1995). Crenulated seafloor: evidence for spreading-rate dependent structure of mantle upwelling and melting beneath a mid-ocean spreading center. *Earth Planet. Sci. Lett.* **129**:73--84

Phipps Morgan J, Sandwell DT. (1994). Systematics of ridge propagation south of 30°S. *Earth Planet. Sci. Lett.* **121**:245--58

Polzin, K. L., Toole, J. M., Ledwell, J. R., and Schmitt, R. W. (1997). Spatial variability of turbulent mixing in the abyssal ocean. *Science* **276**, 93-96.

Ramillien, G., and Cazenave, A. (1997). Global bathymetry derived from altimeter data of the ERS-1 Geodetic Mission. *J. Geodynamics* **23**, 129-149.

Raney, K., The delay/Doppler radar altimeter, *IEEE Trans on Geosciences and Remote Sensing***, v. 36,** N0. 5, p. 1578-1588, 1998.

Rapp, R. H., and Yi, Y. (1997). Role of ocean variability and dynamic topography in the recovery of the mean sea surface and gravity anomalies from satellite altimeter data. *J. Geodesy* **71**, 617-629.

Ribe, N. M. (1982). On the interpretation of frequency response functions for oceanic gravity and bathymetry. *Geophys. J. R. Astron. Soc*. **70**, 273-294.

Ribe NM, Watts AB. (1982). The distribution of intraplate volcanism in the Pacific Ocean basin: a spectral approach. *Geophys. J. Roy. Astron. Soc*. **71**:333--362

Rodriguez, E., and Martin, J. M. (1994). Assessment of the TOPEX altimeter performance using waveform retracking. *J. Geophys. Res*. **99**, 24,957-24,969.

Sahabi M, Géli L, Olivet J-L, Gilg-Capar L, Roult G, et al. (1996). Morphological reorganization within the Pacific-Antarctic Discordance. *Earth Planet. Sci. Lett.* **137**:157--73

Sandwell, D. T. (1982). Thermal isostasy: response of a moving lithosphere to a distributed heat source. *J. Geophys. Res.* **87**: 1001–1014

Sandwell, D. T. (1984). A detailed view of the South Pacific from satellite altimetry. *J. Geophys. Res*. **89**, 1089-1104.

Sandwell, D. T. (1991). Geophysical applications of satellite altimetry. *Rev. Geophys. Suppl*. **29**, 132-137.

Sandwell, D. T. (1992). Antarctic marine gravity field from high-density satellite altimetry. *Geophys. J. Int*. **109**, 437-448.

Sandwell DT, McAdoo DC. (1990). High-accuracy, high-resolution gravity profiles from two years of the Geosat exact repeat mission. *J. Geophys. Res.* **95**:3049--60

Sandwell, D. T., and Smith, W. H. F. (1997). Marine gravity anomaly from Geosat and ERS-1 satellite altimetry. *J. Geophys. Res*. **102**, 10,039-10,054.

Sandwell, D. T. and W. H. F. Smith, (2001). Bathymetric Estimation, *in Satellite Altimetry and Earth Sciences*, edited by L.-L. Fu and A. Cazenave, Intl. Geophys. Series., vol **69**, Academic Press, New York, 441-457.

Sandwell, D. T., and Zhang, B. (1989). Global mesoscale variability from the Geosat exact repeat mission: Correlation with ocean depth. *J. Geophys. Res*. **94**, 17,971-17,984.

Sichoix, L., and Bonneville, A. (1996). Prediction of bathymetry in French Polynesia constrained by shipboard data. *Geophys. Res. Lett*., **23**, 2469-2472.

Shaw, P. R. and S. C. Cande, (1990). High resolution inversion for South Atlantic plate kinematics using joint altimeter and magnetic anomaly data, *J. Geophys. Res., 95*, 2625-2644.

Sleep NH. (1969). Sensitivity of heat flow and gravity to the mechanism of seafloor spreading. *J. Geophys. Res*. **74**:542--9

Small, C. (1994). A global analysis of mid-ocean ridge axial topography. *Geophys. J. Int*. **116**, 64-84.

Small, C., (1994). Imaging mid-ocean ridge transitions with satellite gravity, *Geology*, *22*, 123-126.

Small C and Sandwell, D.T. (1989). An abrupt change in ridge axis gravity with spreading rate. *J. Geophys. Res*. **94**:17383--92

Small, C. (1994) Sandwell, D.T. (1994). Imaging mid-ocean ridge transitions with satellite gravity, *Geology*, **22**, p. 123-126.

Smith, W. H. F. (1993). On the accuracy of digital bathymetry data. *J. Geophys. Res*. **98**, 9591-9603.

Smith, W. H. F. (1998). Seafloor tectonic fabric from satellite altimetry. *Ann. Rev. Earth Planet. Sci.* **26**, 697-738.

Smith, W. H. F., and Sandwell, D. T. (1994). Bathymetric prediction from dense satellite altimetry and sparse shipboard bathymetry. *J. Geophys. Res*. **99**, 21,803-21,824.

Smith, W. H. F., and Sandwell, D. T. (1997). Global seafloor topography from satellite altimetry and ship depth soundings. *Science* **277**, 1956-1961.

Smith WHF, Staudigel H, Watts AB, Pringle MS. (1989). The Magellan Seamounts: Early Cretaceous record of the South Pacific isotopic and thermal anomaly. *J. Geophys. Res*. 94:10501—23.

Smith et al., 2000

Smith, W. H. F., and Wessel, P. (1990). Gridding with continuous curvature splines in tension. *Geophysics* **55**, 293-305.

Stammer, D., (1998). On eddy characteristics, eddy transports, and mean flow properties, J. Phys. Oceanogr., **28**, 727-739.

Stewart, R. H. (1985) "Methods of Satellite Oceanography." University of California Press, Berkeley.

Tapley, B. and Kim, (2001). Applications to Geodesy, *in Satellite Altimetry and Earth Sciences*, edited by L.-L. Fu and A. Cazenave, Intl. Geophys. Series., vol **69**, Academic Press, New York, 371-403.

Tapley, B. D., Chambers, D. P., Shum, C. K., Eanes, R. J., Ries, J. C., and Stewart, R. H. (1994). Accuracy assessment of large-scale dynamic ocean topography from Topex/Poseidon altimetry. *J. Geophys. Res*. **99**, 24,605-24,617.

Tapponier P, Francheteau J. (1978). Necking of the lithosphere and the mechanics of slowly accreting plate boundaries. *J. Geophys. Res*. **8**3:3955--70

Turcotte DL, Schubert G. (1982). *Geodynamics*. New York: John Wiley & Sons. 450 pp.

Vening Meinesz FA. (1941). Gravity over the Hawaiian Archipelago and over the Madiera area: Conclusions about the Earth's crust. *Proc. Kon. Ned. Akad. Wetensia*. 44pp.

Van Wychouse, 1973.

Walsh, E. J., Uliana, E. A., and Yaplee, B. S. (1978). Ocean wave height measured by a high resolution pulse-limited radar altimeter. *Boundary-Layer Meterology* **13**, 263-276.

Watts, A. B. (1978). An analysis of isostasy in the world's oceans: 1, Hawaiian-Emperor seamount chain. *J. Geophys. Res*. **83**, 5989-6004.

Watts, A. B. (1979). On geoid heights derived from Geos-3 altimeter data and flexure of the lithosphere along the Hawaiian-Emperor seamount chain. *J. Geophys. Res*. **38**, 119-141.

Wessel, P., and Smith, W. H. F. (1991). Free software helps map and display data. *EOS Trans. AGU* **72**, 445-446.

Wessel, P., and Smith, W. H. F. (1996). A global, self-consistent, hierarchical, high-resolution shoreline database. *J. Geophys. Res*. **101**, 8741-8743.

Wessel, P., and A. B. Watts, A. B. (1988). On the accuracy of marine gravity measurements. *J. Geophys. Res*. **93**, 393-413.

Walcott RI. (1970). Flexure of the lithosphere at Hawaii. *Tectonophys***. 9**:435--46

Walcott RI. (1976). Lithospheric flexure, analysis of gravity anomalies, and the propagation of seamount chains, in *The Geophysics of the Pacific Ocean Basin and its Margins*, Geophys. Monogr. Ser. vol. 19, ed. by GH Sutton, MH Manghnani, and R. Moberly, pp. 431--8, Washington: Amer. Geophys. Un.

Watts AB. (1978). An analysis of isostasy in the world's oceans 1. Hawaiian-Emperor Seamount chain. *J. Geophys. Res.* **83**:5989--6004

Watts, A. B. (1979). On geoid heights derived from Geos 3 altimeter data along the Hawaiian-Emperor seamount chain. *J. Geophys. Res*. **84**: 3817–3826

Watts AB. (1983). The strength of the Earth's crust. *Marine Technol. Soc. J.* **17**:5--17

Watts AB, Cochran JR. (1974). Gravity anomalies and flexure of the lithosphere along the Hawaiian-Emperor seamount chain. *Geophys. J. Roy. Astron. Soc*. **38**:119--41

Watts AB, Ribe NM. (1984). On geoid heights and flexure of the lithosphere at seamounts. *J. Geophys. Res*. **89**:11152-70

Watts AB, Bodine JH, Ribe NM. (1980). Observations of flexure and the geological evolution of the Pacific Ocean basin. *Nature* **283**:532--7

Wessel P, Watts AB. (1988). On the accuracy of marine gravity measurements. *J. Geophys. Res.* **93**:393--413

Wessel, P. (1992). Thermal stresses and the bimodal distribution of elastic thickness estimates of the oceanic lithosphere. *J. Geophys. Res*. **97**: 14177–14193.

Wessel P, Lyons S. (1997). Distribution of large Pacific seamounts from Geosat/ERS 1: implications for the history of intraplate volcanism. *J. Geophys. Res.* **102**:22459--75

Yale, M. M. (1997). Modeling Upper mantle Rheology with Numerical Experiments and Mapping Marine Gravity with Satellite Altimetry. Ph.D. Thesis, University of Calififormia, San Diego.

Yale, M. M., Gille, S. T., and Sandwell, D. T. (1998). Ocean mixing- mesoscale EKE, bathymetry, and seafloor roughness seen by ERS-1/2 and Topex. *EOS Trans. AGU* **79**, F213.

Yale, M. M., Sandwell, D. T., and Smith, W. H. F. (1995). Comparison of along-track resolution of stacked Geosat, ERS-1 and TOPEX satellite altimeters. *J. Geophys. Res*. **100**, 15,117-15,127.

Yale, M. M., D. T. Sandwell and A. T. Herring, What are the limitations of satellite altimetry?, The Leading Edge, January, 1998, p. 73-76.

Yeh, (1998).